Journal of Petrology

Brown amphibole as tracer of tectono-magmatic evolution of the Atlantis Bank Oceanic Core Complex (IODP Hole U1473A)

Journal:	*Journal of Petrology*
Manuscript ID	Draft
Manuscript Type:	Original Manuscript
Date Submitted by the Author:	n/a
Complete List of Authors:	Ferrando, Carlotta; Università di Pavia, Dipartimento di Scienze della Terra Tribuzio, Riccardo; Università di Pavia, Dipartimento di Scienze della Terra e dell'Ambiente; CNR-IGG, Sezione Pavia Lissenberg, C.; Cardiff University, School of Earth Sciences France, Lydéric; CRPG, MacLeod, Christopher; Cardiff University Basch, Valentin; CNR-IGG, Sezione Pavia Villeneuve, Johan ; CRPG Deloule, Etienne; CRPG Sanfilippo, Alessio; Università degli studi di Pavia, Dipartimento di Scienze della Terra e dell'Ambiente; CNR-IGG, Sezione Pavia
Keyword:	late-stage MORB, melt migration, mineral chemistry, oxygen isotopes, mylonite, lower oceanic crust
Journal of Petrology now offers Virtual Collections of published papers. You may choose up to three collections from the list below. Virtual collections will increase the visibility of your work.:	Mid-Ocean Ridges < Province Themes, Oceanic Crustal Genesis and Evolution < Process Themes

Brown amphibole as tracer of tectono-magmatic evolution of the Atlantis Bank Oceanic Core Complex (IODP Hole U1473A)

Carlotta Ferrando[1]*, Riccardo Tribuzio[1,2], C. Johan Lissenberg[3], Lydéric France[4], Christopher J. MacLeod[3], Valentin Basch[2], Johan Villeneuve[4], Etienne Deloule[4], Alessio Sanfilippo[1,2]

[1] Dipartimento di Scienze della Terra e dell'Ambiente, Università di Pavia, I-27100 Pavia, Italy;
ottaferrando@gmail.com; tribuzio@crystal.unipv.it; alessio.sanfilippo@unipv.it
[2] Istituto Geoscienze e Georisorse, Unità di Pavia, CNR, Pavia, Italy
valentin.basch@gmail.com
[3] School of Earth and Ocean Sciences, Cardiff University, Cardiff, United Kingdom.
LissenbergCJ@cardiff.ac.uk; macleod@cardiff.ac.uk
[4] Université de Lorraine, CNRS, CRPG, F-54000 Nancy, France.
lyderic.france@univ-lorraine.fr; johan.villeneuve@univ-lorraine.fr; etienne.deloule@univ-lorraine.fr

Corresponding author:
* Carlotta Ferrando, Ph.D.
ottaferrando@gmail.com
Dipartimento di Scienze della Terra e dell’Ambiente, University of Pavia
Via Ferrata 1, 27100 Pavia, Italy

Abstract

Brown amphibole is a minor but common mineral component in lower oceanic crust. It is generally interpreted as products of migrating SiO_2 and H_2O-rich fluids or melts, which can be either residual melts from advanced magmatic differentiation of Mid-Ocean Ridge Basalt (MORB), or hydrothermal fluids including a seawater component. Within the lower oceanic crust exhumed at the Atlantis Bank Oceanic Core Complex (OCC), along the ultraslow Southwest Indian Ridge, brown amphiboles is ubiquitous in all lithologies from olivine- to oxide-gabbros and diorites, including both undeformed and plastically deformed varieties. We here show the results of a systematic petrological study conceived to unravel the nature of the H_2O-rich component recorded in brown amphiboles and document: *(i)* the evolution of migrating melts during the magmatic stage and *(ii)* different extents of melt-bearing deformation events recorded throughout the entire crustal transect. The low Cl contents and the light over heavy Rare Earth Elements (LREE/HREE) ratios and high Ti contents in brown amphiboles, indicate they crystallized from melts with a magmatic hydrous component. Consistently, their $\delta^{18}O$ values are in equilibrium with MORB composition, except for diorite amphiboles that possibly record the local assimilation of altered minerals. In undeformed olivine gabbros, interstitial pargasite crystallized at hypersolidus conditions (~1000°C) from the melt residual after late stages of MORB differentiation. We speculate that before the olivine gabbro crystal mush reached fully solid state, some aliquots of residual melts were extracted to form discrete intervals of oxide gabbros. There, ferrobasaltic melts differentiated through the early crystallization of Fe-Ti oxides and clinopyroxene as liquidus phases. This process promoted rapid Si enrichment and depletion in Fe, Ti, V in the residual melt, later extracted to form the crosscutting diorite veins. The mylonitic olivine gabbros record high-temperature plastic deformation (~900°C ± 50°C), initiated at hypersolidus conditions involving melts residual from previous crystallization of the gabbroic rock. Further solid-state plastic deformation led to substantial grain-size reduction and, consequently, to an increase in porosity. This created pathways for subsequent melt focussing, which likely represent late-stage differentiated melts migrating throughout the lower crustal section. This study shows that brown amphibole in the Atlantis Bank lower oceanic crust is the crystallization product of melts residual from advanced magmatic differentiation, which are also locally involved in the plastic deformation events during crustal accretion.

Keywords: *lower oceanic crust; late-stage MORB; melt migration; mineral chemistry; oxygen isotopes; mylonite*

INTRODUCTION

Calcic brown amphibole, mostly of pargasitic or edenitic compositions (classification by Leak et al., 1997), is a minor but ubiquitously distributed mineral phase in sections of oceanic crustal sequences (e.g., Coogan et al., 2001; Gillis & Meyer, 2001; Niu et al., 2002; Miranda & John, 2010; Tamura et al., 2016; Nguyen et al., 2018; Gardner et al., 2020) and ophiolite analogues (e.g., Tribuzio et al., 1995, 1999, 2000, 2020; Cortesogno et al., 2000). It is the main hydrous mineral precipitating at high temperature conditions (>600°C) in MOR settings. This peculiarity makes it fundamental marker of processes shaping the lower oceanic crust and a unique tracer of geochemical exchanges between the Earth interior and the hydrosphere.

In mid-ocean ridge (MOR) environments, because primitive MORB are overall nearly dry (on average H_2O <0.2 wt%; Sobolev & Chaussidon, 1996), the stability of hydrous phases can be achieved either by advanced fractionation of anhydrous phases (i.e., magmatic differentiation of MORBs; see Koepke et al., 2018) or by addition of seawater-derived fluids (see Koepke et al., 2004). Various amphibole textural occurrences were documented in MOR settings; they may appear as interstitial phase in undeformed gabbroic rocks, as coronas partially replacing clinopyroxene crystals, or as subhedral crystals in crosscutting amphibole veins, as well as in association with neoblastic assemblage within mylonitic intervals. These multiple textural occurrences and the extremely variable chemical compositions that brown amphibole can assume are commonly interpreted as resulting from solidification of late-stage differentiated melts (e.g., Coogan et al., 2001; Gillis & Meyer, 2001; Niu et al., 2002), or metasomatism by Si- and water-rich fluids (e.g., Tribuzio et al., 1995; Coogan et al., 2001; Gillis & Meyer, 2001; Miranda & John, 2010; Nicollet et al., 2022). Discriminating between the magmatic or hydrothermal origin of the brown amphibole remains widely debated and is, however, not straightforward (see Coogan et al., 2001; Gillis & Meyer, 2001). The complexity in interpreting their formation is tangled by the stability of brown amphibole over a wide range of temperatures and by the fact that it may crystallize during (melt-assisted) plastic deformation under granulite-facies (800°C-950°C) to amphibolite-facies (590°C-800°C) conditions (e.g., Miranda & John, 2010; Gardner et al., 2020). If we can unravel the origin of brown amphibole, we can gain crucial understanding of the evolution of magmatic systems beneath MOR and untangle the tectonic processes involved in the exhumation of lower oceanic crustal sequences.

At ~57°E along the Southwest Indian Ridge (SWIR), a long-lived detachment fault has exhumed a >1500 m-thick section of lower oceanic crust, now forming the domal structure of the Atlantis Bank Oceanic Core Complex. The Atlantis Bank plutonic section formed through protracted accretion of intermittent intrusions (Dick et al., 2019a; Boulanger et al., 2020) and subsequent upward melt migration (Dick et al., 2000; Natland and Dick, 2001; Sanfilippo et al., 2020; Zhang et al., 2020; Boulanger et al., 2021; Ferrando et al., 2021a,b) in a complex dynamic environment during ongoing seafloor extension. Continuous exhumation and cooling of the lower crustal section led to progressive deformation mechanisms under decreasing temperature conditions (Miranda & John, 2010; Gardner et al., 2020; Taufner et al., 2021). Within this lower oceanic crustal sequence, brown amphibole has been identified in nearly all lithologies and in both undeformed and deformed intervals (Dick et al., 2000; MacLeod et al., 2017; Zhang et al., 2020). Most studies focused on the origin of these amphiboles occurring in such different lithologies (e.g., Coogan et al., 2000; Gillis & Meyer, 2001), but little attention has been paid to their implications for magmatic and high-temperature deformation history of the Atlantis Bank OCC.

In the present study, we conduct a petrological and geochemical investigation of brown amphibole in undeformed and deformed gabbroic rocks. Undeformed samples span all lithologies recovered, from most primitive olivine gabbros to more evolved oxide gabbros and diorites, whereas plastically deformed samples are mylonitic olivine gabbros. Textural relationships and mineral chemistry, together with their $\delta^{18}O$ compositions indicate that brown amphiboles from undeformed and mylonitic olivine gabbros are of magmatic origin. The amphibole chemical compositions allow us to reconstruct the magmatic evolution of late-stage differentiated melts residual from olivine gabbro crystallization. We show how partial extraction of these residual melts lead to oxide gabbro formation and subsequent emplacement of diorite veins. The evident involvement of interstitial trapped melts in plastically deformed olivine gabbros is in line with initiation of detachment faulting at hypersolidus conditions. On the other hand, we show that infiltration of external melts also occurred within previously deformed intervals, with no evidence of further strain localization.

THE ATLANTIS BANK OCEANIC CORE COMPLEX

Geological setting

The ultraslow SWIR spreads approximately at a full rate of 14 mm/yr and trends SW-NE, oblique to its N-S spreading direction. At 57° E, the Atlantis II Transform offsets the ridge axis of ~200 km. Along the transverse ridge east of the transform valley, the Atlantis Bank is the shallowest and northernmost domal structure (Fig. 1a). This dome is a large Oceanic Core Complex (OCC) that exposes lower oceanic crustal rocks and lithospheric mantle on the seafloor, exhumed by an 11–13 Myr old long-lived oceanic detachment fault (e.g., Dick et al., 1991; Dick et al., 2000). The Atlantis Bank plutonic section formed by successive magma emplacement for ~3 Myr (Dick et al., 1991; John et al., 2004; Schwartz et al., 2005; Rioux et al., 2016). Initially uplifted at the ridge-transform intersection, a 10° counterclockwise change in regional spreading direction put the transform into transtension resulting in additional uplift of the Atlantis Bank OCC and formation of a tectonic island capped by a carbonate platform (Dick et al., 1991; Baines et al., 2007; Baines et al., 2008) at ~7 Ma (Palmiotto et al., 2013, 2017), which is now mostly eroded. The highly asymmetric spreading of 9.8 mm/yr to the south and 4.9 mm/yr to the north transposed the Atlantis Bank to its actual position ~80 km south of the ridge (Baines et al., 2008; Fig. 1a).

Several site surveys and sampling expeditions investigated the Atlantis Bank structure in the past 30 years. Previous Ocean Drilling Program (ODP) operations drilled the 1508m-deep Hole 735B and the 150m-deep Hole 1105A (Dick et al., 1991; Dick et al., 2000; Pettigrew et al., 1999), and more recent International Ocean Discovery Program (IODP) Expedition 360 drilled the 800m-deep Hole U1473A (MacLeod et al., 2017). ROV and submersible dives and dredging (Dick et al., 2019a) also sampled rocks that compose the dome, revealing a heterogeneous vertical and lateral structure. Serpentinized mantle peridotites were found along the east of the transform wall, whereas no evidence of mantle screens was found in the plutonic sector of the Atlantis Bank OCC (Dick et al., 2019a). Based on lithologies recovered in the deepest Hole 735B, the core of the massif appears to be mostly composed of olivine gabbro to gabbro, with minor chemically primitive (e.g., troctolites) and more evolved lithologies (e.g., oxide gabbros) (Fig. 1b). Upwardly differentiated olivine gabbro chemistry within discrete intervals demonstrates that the lower oceanic crust was built by successive and intermittent magmatic intrusions (Dick et al., 2000; Dick et al., 2019a). Porous flow and magmatic crystallization within the lower oceanic crust led to a progressively chemical evolution of intercumulus melts, which migrated and were expulsed from the inner to the outer portions of the Atlantis Bank (Dick et al., 2000; Natland and Dick, 2001; Sanfilippo et al., 2020; Zhang et al., 2020), as testified by the upward and lateral increase in modal abundance of oxide gabbros (oxide cap; Dick et al., 2019a; Boulanger et al., 2020; Fig. 1b).

Melt migration persisted under hypersolidus conditions, once the gabbros nearly reached a solid state. Deformation related to the continuous oceanic crustal exhumation by detachment faulting (Miranda & John, 2010; MacLeod et al., 2017) localized Fe-Ti rich intercumulus melts into mylonitic shear zones (e.g., Natland & Dick, 2001; Zhang et al., 2020; Gardner et al., 2020), as evidenced by the common occurrence of oxide-rich material within highly strained zones in the upper ~500 mbsf. The involvement of melt into deformed horizons demonstrate that initiation of the detachment fault started at depth in partially molten gabbro (Dick et al. 1991a; Dick et al. 2000). Mylonites also record a sequence of deformation mechanism from high-temperature (800°C-950°C) to lower temperature (590°C-800°C) conditions (Miranda & John, 2010), attesting that the tectonic evolution continued under decreasing temperature conditions. Although some amounts of amphibole are typically present in most mylonitic samples, calculated temperatures indicate that ongoing plastic deformation developed under granulite-facies, marked by the plagioclase + pyroxene neoblastic assemblage ± brown amphibole, to amphibolite-facies conditions mainly consisting of brown amphibole + plagioclase. Here, following the Shipboard records (see MacLeod et al., 2017) we use the same facies classification.

The lower gabbroic crust in Hole U1473A

IODP Hole U1473A was drilled into the flat summit of Atlantis Bank OCC during IODP Expedition 360 (MacLeod et al., 2017) and further deepened during IODP Expedition 362T to a current total depth of 809.4 m below seafloor (mbsf; Blum et al., 2017). The recovered section of lower oceanic crust (Fig. 2) is mainly composed of olivine gabbros (76.5% of recovery) interspersed at different depths with evolved gabbro *sensu stricto* (5% of recovery) and oxide-bearing gabbroic rocks (17% of recovery). The gabbroic lithologies are crosscut by felsic veins and rare diabase dykes (total of 1.5% of recovery). Downhole bulk-rock chemical compositions determined onboard the R/V *JOIDES Resolution* outline two major trends of upward decrease in Mg# (Fig. 2), Ca#, and Cr and Ni concentrations coupled with increase in Ti and Y contents (Dick et al., 2019b), defining two main chemical units bounded by two geochemical discontinuities (at ~60–90 mbsf and ~350 mbsf). These chemical units in Hole U1473A were interpreted as upward-differentiated magmatic intrusive units.

Although static hydrothermal alteration occurred pervasively throughout Hole U1473A, it slight decreases within the deepest portion of the section (Fig. 2). Alteration mineral abundance is on average <30%; however, widespread intervals of <3% alteration occur, in which the original magmatic fabrics and textures are well preserved (MacLeod et al., 2017; Fig. 2). *Gabbros* are commonly isotropic or display weak plagioclase shape preferred orientations, thus lacking well-developed magmatic fabrics (MacLeod et al., 2017; Fig. 3a-b). Grain-size variations, from fine-grained granular domains to coarse-grained subophitic intervals, are a ubiquitous textural feature of gabbros throughout the hole. The most widespread 'patchy' grain size variations have been interpreted as the result of compaction-aided melt extraction from the coarse-grained intervals and concomitant melt accumulation in discrete domains where fine-grained gabbros rapidly formed (Ferrando et al., 2021a,b). At about 150 and 600 mbsf, the grain-size heterogeneities define decimeter-scale igneous layering that was interpreted as results of interfingered intrusive events of distinct magmas (Boulanger et al., 2021; Pieterek et al., 2022).

In coarse-grained intervals of *olivine gabbros*, subophitic clinopyroxene commonly embay elongated and partially corroded plagioclase crystals, attesting that chemical disequilibrium triggered partial dissolution of plagioclase and crystallization of clinopyroxene (Sanfilippo et al., 2020). Mineral chemical compositions reveal that magma emplacement, melt extraction and accumulation processes are accompanied by melt reactive percolation (see also Zhang et al., 2020; Boulanger et al., 2021; Ferrando et al., 2021a). Clinopyroxene crystals, mostly coarse- and medium-grained, display core-to-rim selective enrichments in highly incompatible trace elements relative to less incompatible trace elements (i.e., Ce to Y; Zr to Nd), similar to trace element zoning patterns documented in clinopyroxenes from gabbroic lithologies recovered in the adjacent Hole 735B (Gao et al., 2007; Lissenberg and MacLeod et al., 2016; Boulanger et al., 2020; Zhang et al., 2021). These grain-scale observations were interpreted as resulting from dissolution–reprecipitation reactions between migrating melts and a primitive crystal mush.

Oxide-bearing gabbroic rocks (sensu lato; >1% Fe-Ti oxide phases) are widespread in the entire lower crustal section in Hole U1473A, contrasting with oxide-rich layer concentrated in the shallowest 600 m of Hole 735B. Oxide gabbros often occur in centimeter-scale intervals in crosscutting relationships with the olivine gabbros throughout Hole U1473A (Dick et al., 2019b). They are mostly undeformed in the deepest part of Hole U1473A, whereas they tend to be plastically deformed throughout the hole being localized in variably thick shear zones.

Felsic veins, including diorite, quartz diorite, leucodiorite, tonalite, and trondhjemite, are often associated with reaction halos into the host gabbroic rocks, as evidenced by the formation of brown amphibole around clinopyroxene and the change in plagioclase chemistry to a more sodic composition (MacLeod et al., 2017). Contacts between felsic material and host gabbro range from diffuse to sharp. The origin of the different generations of felsic veins appears to be correlated with lower crustal exhumation during emplacement of the OCC. Felsic veins with generally diffuse boundaries, high magnetite/ilmenite ratios and low amphibole Cl/F ratio were interpreted to have formed by fractional crystallization under high-temperature conditions (Nguyen et al., 2018; Ma et al., 2020). Conversely, felsic veins with sharp boundaries and high amphibole Cl/F ratio formed by hydrous melting (anatexis) as a consequence of melt intrusion in hydrothermally altered gabbros (Ma et al., 2020).

Most of the lower crustal section in Hole U1473A underwent some extent of crystal-plastic deformation (e.g., Allard et al., 2021). Crystal-plastic fabrics are irregularly spaced and locally pervasive (Fig. 3c), with overall high intensity, decreasing solely within the deepest 200m of the hole (Fig. 2). Mylonitic shear zones are copious (crystal plastic fabric intensity of 4 out of 5; Fig. 2), locally grading into ultramylonite horizons (crystal plastic fabric intensity of 5; see Fig. 2, 3a; MacLeod et al., 2017). Crystal plastic fabrics are defined by lens-shaped plagioclase, clinopyroxene and minor olivine porphyroclasts mantled by granulite-facies neoblast assemblages of olivine, plagioclase, clinopyroxene, ilmenite (Fe-Ti oxide phases) and subordinate orthopyroxene; neoblasts also locally include brown amphibole (MacLeod et al, 2017). Many granulite-facies mylonites display Fe-Ti oxide segregations elongated parallel to the foliation plane, which were interpreted as tracer of evolved melts migrating within the mylonitic horizon (MacLeod et al., 2017; Taufner et al., 2021).

Less commonly, some neoblast assemblages are composed of plagioclase and brown-green amphibole (i.e. hornblende) formed under lower-amphibolite-facies conditions. This finding of amphibole-facies shear zones down to deep levels in Hole U1473A (down to 670 mbsf) suggests that shear zones may have acted as preferential pathways for hydrothermal fluids (MacLeod et al., 2017). Other possible fluid pathways are the amphibole veins, mostly localized within the first ~250 mbsf of the hole.

SAMPLING AND ANALYTICAL METHODS

Sample overview

Undeformed and deformed gabbros of diverse compositions were selected for petrographic investigations and chemical analyses. These samples display minor moderate- to low-temperature alteration products, mainly localized in olivine with common mesh textures filled with talc, serpentine, and magnetite. In the oxide gabbros, pale-green amphibole locally replaces brown amphibole at the crystal rim, although the core still preserves dark- to light-brown pleochroism. In this study, we exclusively investigate textural and compositional characteristics of brown amphibole.

We selected eight undeformed samples preserving magmatic microstructural characteristics: three olivine gabbros (U1473A-89R-1W, 14-20cm, depth: 779.3 mbsf; U1473A-89R-1W, 86-93cm, depth: 779.4 mbsf; U1473A-89R-6W, 4-9cm, depth: 785.9) and three oxide gabbros (U1473A-81R-3W, 77-82cm, depth: 715.8 mbsf; U1473A-83R-1W, 13-20cm, depth: 730.8 mbsf; U1473A-85R-3W, 38-41cm, depth: 753.6 mbsf) within the deepest portion of IODP Hole U1473A; two diorites from both deep and shallow portions of the hole (U1473A-39R-4W, 3-8cm, depth: 356 mbsf; U1473A-89R-3W, 108-110cm, depth: 783 mbsf). Olivine gabbros display typical subophitic textures characterized by poikilitic clinopyroxene embaying subhedral to partially corroded plagioclase and rarely anhedral olivine (Fig. 4a). Oxide gabbros show hypidiomorphic textures with large subhedral pyroxenes and plagioclase, >10 vol% of anhedral to skeletal Fe-Ti oxides and interstitial amphibole crystals (Fig. 4f). One sample of oxide gabbro displays large interstitial amphibole associated with large euhedral apatite crystals (U1473A-83R-1W, 13-20cm; Fig. 4g). Diorites are decimetre-thick veins crosscutting gabbros with sharp but undulating boundaries (Fig. 5a). Diorites are composed of euhedral plagioclase, poikilitic amphibole, Fe-Ti oxides and minor small euhedral apatite crystals, and do not contain clinopyroxene (Fig. 5b,c). Along the diorite-host gabbro contact, amphibole rims clinopyroxene from the host gabbro (Fig. 5a). The host gabbro displays poikilitic textures and incipient re-crystallization of plagioclase and clinopyroxene along the grain boundaries.

Two mylonitic olivine gabbros were also selected. Samples show porphyroclastic textures with well-developed crystal-plastic foliation. The first mylonite is from 378.8 mbsf (U1473A-41R-6W, 23-29 cm) and includes thin levels composed of a fine-grained association of Fe-Ti oxides, apatite, and amphibole undeformed crystals (Fig. 6). Deeper in the hole, the second mylonite was sampled at 624.8 mbsf (U1473A-69R-1W, 23-28cm) and displays a ~7 mm-thick oxide gabbronoritic band crosscutting the porphyroclastic foliation at a low angle (~6°) (Fig. 7).

Chemical maps and *in situ* analyses

Chemical maps of whole thin sections were acquired for two samples of olivine gabbros and the two mylonitic gabbros. We used the Zeiss Sigma HD field emission gun equipped with dual 150mm^2 Oxford Instruments X-Max^N energy dispersive silicon drift detectors installed at Cardiff University. This machine enables high count rates (>1,000,000 cps) and rapid acquisition of both qualitative and quantitative element maps of all phases, here at 30 µm step ("pixel") size. The data were background-corrected using Oxford Instruments AZtec software prior to the processing of element maps and statistical analysis by using the python-based tool 'Quantitative Assessment of Compositional Distribution (QACD)', which quantifies element ratios as An in plagioclase and Mg# in olivine, pyroxenes and amphibole (Loocke, 2016).

Amphibole, clinopyroxene and plagioclase from all samples were analysed *in situ* for Si, Ti, Al, Cr, Fe, Mn, Ni, Mg, Ca, Na and K (Supplementary Data Table S1) by electron microprobe (JEOL 8200 Super Probe) operating at Dipartimento di Scienze della Terra, University of Milano, in wavelength dispersive spectrometry mode. We also analysed Cl in amphibole from all samples. The analyses were performed with 30s counting time on the peak (10s on the backgrounds) and 1µm spot size, at 15 kV accelerating potential and 15 nA beam current. Natural minerals and synthetic oxides were used as standards. The Mg-values of amphibole and clinopyroxene was calculated as $Mg\# = Mg/(Mg + Fe^{2+}_{tot})x100$ and the anorthite contents in plagioclase as $An = Ca/(Ca+Na+K)x100$.

In situ trace elements contents in amphibole, clinopyroxene and plagioclase were obtained using Laser Ablation Inductively Coupled Plasma Mass Spectrometry (LA-ICP-MS) at C.N.R., Istituto di Geoscienze e Georisorse (Unità di Pavia; Supplementary Data Table S2). We measured Sc, Ti, V, Cr, Co, Ni, Zn, Rb, Sr, Y, Zr, Nb, Ba, La, Ce, Pr, Nd, Sm, Eu, Gd, Tb, Dy, Ho, Er, Tm, Yb, Lu, Hf, Ta, Pb, Th, U. Clinopyroxene and plagioclase were analysed using a Q-switched Nd:YAG laser, model Quantel (Brilliant) with 213 nm wavelength and a fluence of ~9.5 J/cm^2. The laser was operated at 10 Hz frequency, with a pulse energy of 35 mJ and spot diameter typically of 50-75 µm for clinopyroxene and 100-120 µm for plagioclase. Amphibole grains were ablated using an ArF excimer laser microprobe at 193 nm (Geolas200Q-Microlas) with a spot size of 35-50 µm. The ablated material was analysed by using a PerkinElmer SCIEX ELAN DRC-e quadrupole mass spectrometer using Helium as carrier gas mixed with Ar downstream of the ablation cell. Data reduction was performed using the GLITTER software

(Van Achterbergh et al., 2001), using the linear fit to ratio method. Concentrations were calibrated against the NIST SRM 612 rhyolitic synthetic glass using the values given in Pearce et al. (1997). ^{43}Ca was used for internal standardization relative to EPMA data. Precision and accuracy were assessed from repeated analyses of the BCR-2g reference material and resulted usually better than 10%.

Oxygen isotopes in amphibole crystals were measured *in-situ* for undeformed olivine gabbros, diorites and the mylonitic olivine gabbros (Supplementary Data Table S3) using the Cameca IMS-1270 E7 ion microprobe at the 'Centre de Recherches Pétrographiques et Géochimiques' (CRPG-CNRS) in Nancy (France). A focused primary beam of Cs^+ was used with an intensity of 2.5 nA, and a spot size of ~15 µm. Each analysis consists of 30 cycles. The analysed surface was cleaned by few seconds of pre-sputtering to prevent surface contamination. Two amphiboles of different compositions, one from the Ilímaussaq Complex (Mg# = 0 and $\delta^{18}O = -2.1 \pm 0.19$‰ VSMOW) and another from the Kipawa Syenite Complex (Mg# = 66 and $\delta^{18}O = 7.9 \pm 0.08$‰ VSMOW) were used as standard to correct for instrumental mass fractionation. Five individual standard measurements were performed at the beginning and at the end of every data acquisition blocks usually composed of about 30-35 individual unknown measurements. The overall error calculated for the entire analytical session was less than ±0.25‰ (2σ). To check for possible intra-grain oxygen isotope heterogeneity, as well as to minimize the error of $\delta^{18}O$ determination for each amphibole crystal, at least three spots (and up to 5) in different areas of each selected individual grain were analysed. All points were checked using SEM imaging after analyses to ensure that only amphiboles were analysed.

BROWN AMPHIBOLE TEXTURAL OCCURRENCES AND MINERAL CHEMISTRY

Brown amphibole in Hole U1473A occurs in undeformed (Fig. 4, Fig. 5) and deformed (Fig. 6, Fig. 7) gabbroic rocks, ranging from olivine gabbro (Fig. 4a-e) to more evolved oxide gabbro (Fig. 4f-g) and diorites (Fig. 5). The modal abundance of brown amphibole ranges from <0.1 vol% in olivine-rich gabbro (olivine >10 vol%) to ≤0.5 vol% in olivine gabbro, up to 5 vol% in oxide gabbros, and ~10 vol% in diorites. In mylonites, brown amphibole is overall ≤2 vol%. All analysed brown amphiboles display low Cl contents (<0.03 wt%; Supplementary Data Table S1).

Undeformed olivine gabbros

Brown amphiboles in undeformed olivine gabbros are pargasites (Si a.p.f.u. = 6.2-6.4; Fig. 8) according to the classification of Leake et al. (1997). Pargasite typically occurs as isolated films (≤50µm thick) interstitial to plagioclase, clinopyroxene and olivine (Fig. 4a-c), and are characterized by high Ti contents (TiO_2 >2.2 wt%; Fig. 4b). Their well-defined grain boundaries appear either planar or smoothly curved depending on the shape of adjacent crystals (Fig. 4c). Commonly, pargasite occurs in association with Fe-Ti oxides and/or sulfides (Fig. 4c-d) and locally with µm-size crystals of apatite. Pargasite also forms 'blebs' or lamellae in large clinopyroxene crystals, commonly aligned parallel to the cleavage planes (Fig. 4e). These bleb-shaped amphiboles have planar or irregular but well-defined grain boundaries.

Pargasite in the olivine gabbros display the highest Mg# among all of the studied samples, with values ranging between 66 and 75. It has high CaO (11-12 wt%), Al_2O_3 (10-13 wt%) and TiO_2 (2.3-4.1 wt%), and low MnO (0.1-0.2 wt%), whereas K_2O and Na_2O range in the intervals 0.07-0.3 wt% and 2.2-2.9 wt%, respectively (Fig. 9). Interstitial and bleb-shaped pargasite have comparable compositions, except for K_2O and Na_2O that are slightly higher in bleb-shaped pargasite (Fig. 9). However, bleb-shaped pargasite displays overall slightly higher TiO_2 contents at lower Mg# compared to the interstitial crystals. No additional correlation was observed between the pargasite textural occurrence and their significantly variable TiO_2 contents, which show a negative correlation with pargasite Mg#.

The interstitial pargasite is commonly associated with rims of plagioclase showing low An contents and Fe-rich rims of clinopyroxene. The development of bleb-shaped pargasite in clinopyroxene is locally associated with ~200 µm-thickness rim of orthopyroxene (Fig. 4e). Prismatic euhedral to subhedral plagioclase and poikilitic clinopyroxene are always zoned. An contents in plagioclase range between 51 and 63 mol% and their K_2O contents are <0.1 wt% (Fig. 10a-b), with the highest An contents recorded in the crystal cores (Fig. 11a). Clinopyroxene cores display high Mg# (~80-85) that decrease towards the crystal rims (down to Mg# ~75; Fig. 10c, Fig. 11b, Supplementary Figure S1).

Undeformed oxide gabbros and diorites

Oxide gabbros contain pargasitic to edenitic amphibole (classification of Leake et al., 1997; Si a.p.f.u. = 6.3-6.9; Fig. 8). Pargasites commonly form 50 to 200 µm-thick films with well-defined grain boundaries between large clinopyroxene and plagioclase crystals, and are often associated with ilmenite and/or magnetite (Fig. 4f). They also occur within large pyroxenes as isolated <50µm-size blebs with random orientations and associated with Fe-Ti oxides. Edenites are typically larger anhedral to subhedral grains (up to ~2 mm) associated with orthopyroxene, ilmenite and magnetite. Euhedral grains of apatite are associated with these edenites (Fig. 4g).

Pargasite and edenite from oxide gabbros display lower Mg# (56.8-65.2), CaO (10.3-11 wt%) and Al_2O_3 (7-11 wt%), higher MnO (0.16-0.35 wt%) and K_2O (0.2-0.4 wt%), and similar Na_2O (2-2.7 wt%) and TiO_2 (2-3.4 wt%) contents compared to pargasite from olivine gabbros (Fig. 9). Edenite has higher Mg# (62.8-65.2) and lower Al_2O_3 (6.9-8.9 wt%), TiO_2 (2-2.3 wt%) and Na_2O (2.1-2.36 wt%) compared to its pargasitic counterpart (Supplementary Data Table S1). No chemical distinction can be made between interstitial and bleb-shaped pargasites (Fig. 9).

Brown amphiboles in oxide gabbros are associated with sodic plagioclase rims (An = 34-43), whereas the plagioclase cores typically display slightly higher An contents (An = 40-44). Clinopyroxene is unzoned with Mg# ranging from 67 to 70 (Supplementary Figure S1; Supplementary Data Table S1).

The *internal portion of diorite veins* is characterized by large (up to 4 mm in size) subhedral to poikilitic crystals of edenitic amphibole (classification of Leake et al., 1997; Si a.p.f.u. = 6.5-7.1; Fig. 8), which are associated with ilmenite and magnetite. Poikilitic edenites typically enclose euhedral plagioclase, apatite and zircon (Fig. 5c). Plagioclase also occurs as nearly centimetric subhedral grains.

Compared with brown amphibole from the oxide gabbros, edenite from diorites display similar Mg# and Na_2O contents, whereas Al_2O_3, TiO_2 and K_2O tend to slightly lower contents and MnO is remarkably higher (Fig. 9). The diorite amphiboles have compositions comparable to those of brown amphibole found in various felsic material from Hole U1473A reported in literature (Fig. 9). Plagioclase is zoned with average An ~36 and K_2O contents in the range 0.14-0.18 wt% in crystal cores, and An <30 and K_2O contents overall >0.2 wt% in crystal rims. (Fig. 10a).

The sharp *diorite-host gabbro contact* is marked by coronas of edenitic amphibole on rims of clinopyroxene from the host gabbro. The grain boundary of the coronitic edenite against clinopyroxene is typically irregular and indented (Fig. 5a-b), indicating that amphibole was overgrown on clinopyroxene. The coronitic edenite include abundant euhedral crystals of Fe-Ti oxide phases (Fig. 5b), which is a common phase all along the diorite-host gabbro contact. Within 1 mm from the contact, the primary mineral phases in the host gabbro display strong chemical differentiation. The rim of the clinopyroxene overgrown by the diorite amphibole is remarkably Fe-rich compared with the crystal core (Supplementary Figure S1), and plagioclase displays a core-to-rim enrichment in albitic component. Such enrichments at the plagioclase rim reach compositions similar to those of plagioclase rim in the diorite vein core (Fig. 10a; Supplementary Data Table S1).

Granulite-facies mylonites

Mylonitic olivine gabbro

Nearly equant fine grains (50-100 µm) of pargasite (Si a.p.f.u. = 6.2-6.5; Fig. 8) with no visible plastic deformation form aggregates in mylonitic olivine gabbros (Fig. 6a-b). The pargasite grains are associated with Fe-Ti oxides and micron-scale equigranular neoblasts of clinopyroxene and minor orthopyroxene, which have polygonal morphology with ~120° grain triple junctions (Fig. 6c-d). (Clino)pyroxene neoblasts comprise ~70 vol% of the neoblastic assemblage, whereas pargasite+Fe-Ti oxide cover up to 30 vol% (Fig. 6b). The pyroxenes + pargasite + Fe-Ti oxides neoblastic aggregates are elongated parallel to the crystal-plastic fabric forming tails departing from the clinopyroxene porphyroclasts (Fig. 6c-d). Bands of neoblastic plagioclase displaying equilibrated textures (e.g., triple junctions) parallelly alternate with the mafic bands defining the foliation and mantling the porphyroclasts mainly of clinopyroxene and olivine (Fig. 6a-b). The large porphyroclastic grains display undulose extinction and are internally deformed (Fig. 6d), whereas crystal grains in the neoblastic assemblage are internally undeformed. Apatite crystals of ~200 µm-size associated with mm-size orthopyroxene occur in pressure shadows at the edge of some clinopyroxene porphyroclasts (Fig. 6c-d). The plagioclase-pyroxene ± amphibole neoblastic association documents recrystallization under granulite-facies conditions (following MacLeod et al., 2017).

Elongated aggregates of pargasite also occur in ~200µm-thick isolated bands in association with ilmenite and apatite and are intercalated with thicker bands of plagioclase neoblasts (Fig.

6a,b,e). Along these thin bands, 500 µm-stretched anhedral pargasite crystals occur at the contact with clinopyroxene porphyroclasts (Fig. 6e).

Pargasite in the mylonitic olivine gabbro has compositions comparable with those of undeformed olivine gabbros (sample 41-6 in Fig. 9), with Mg# ranging between 66 and 72 and TiO_2 in the interval 1.8-3.6 wt%. The plagioclase and clinopyroxene neoblasts in association with pargasite have An contents ranging from 42 to 59 (K_2O<0.1 wt%; Fig. 10a-b) and Mg# of 77-80 (Fig. 10c, Supplementary Figure S1), respectively. The plagioclase porphyroclasts tend to be slightly more enriched in An compared to the plagioclase neoblasts (Fig. 11c). The alternating compositional bands of neoblastic plagioclase fall in the compositional range of zoned plagioclase from undeformed olivine gabbro (Fig. 10b), which suggests that this chemical variability was inherited from the magmatic zoning (Fig. 11a,c). Similar to plagioclase, the porphyroclastic clinopyroxenes preserve a primary chemical zonation marked by rims with higher Fe contents (Fig. 11d).

Mylonitic olivine gabbro with oxide gabbronoritic band

Sample U1473A-69R-1W, 23-28cm displays a well-foliated mylonitic olivine gabbro crosscut by a ~7 mm-thick band composed of abundant orthopyroxene (~15 vol%) and neoblastic to anhedral clinopyroxene (~37 vol% in total; see later the distinction in clinopyroxene generations), neoblastic plagioclase (~30 vol%), an assemblage of Fe-Ti oxides + apatite (~15 vol%), and minor pargasite (<3 vol%). Based on its mineralogy, hereafter this band is referred to as 'oxide gabbronoritic band' (Fig. 7a-b). Its host mylonite (Fig. 7a) has typical porphyroclastic textures defined by plagioclase, clinopyroxene and olivine porphyroclasts mantled by pyroxenes + pargasite + Fe-Ti oxides neoblastic aggregates. It is characterized by chemical compositions similar to those of the other granulite-facies mylonitic sample from this study (Fig. 9, Fig. 10, Supplementary Figure S1). Despite such evident similarities, the neoblastic grains within the host mylonite are overall finer (rarely ~100 µm and commonly <50 µm) than those in the other mylonitic olivine gabbro.

From the mylonitic olivine gabbro to the oxide gabbronoritic band, pargasite/orthopyroxene ratio drastically decreases, and modal contents of apatite and ilmenite significantly increase (Fig. 7a-b). The band shows parallel alternations of thin layers of pyroxene + pargasite + plagioclase and pyroxene + plagioclase + Fe-Ti oxide phases + apatite (Fig. 7b). Equigranular and polygonal neoblasts of µm- size pyroxene + pargasite + plagioclase are concentrated along the contact with the host mylonitic olivine gabbro. There, this neoblastic assemblage is characterized by the presence of a mm-long grain of euhedral titanite with well-defined grain boundaries (Fig. 7a-b). Pargasites occur as interstitial to nearly equant grains at pyroxene neoblasts triple junctions (Fig. 7c). The core of the oxide gabbronoritic band is characterized by mm-size euhedral crystals of orthopyroxene mantled by euhedral tens of µm-size grains of apatite associated with Fe-Ti oxides (Fig. 7a-c). There, plagioclase shows subhedral and granular to nearly interstitial habit, whereas clinopyroxene porphyroclasts are overgrown by coronas of secondary clinopyroxene, which have lobate and tortuous grain boundaries with the large clinopyroxene crystals (Fig. 7d). Although these clinopyroxene microstructures are mostly evident within the core of the oxide gabbronorite, they also occur locally along the contact with the host mylonite where secondary clinopyroxene partially overgrew elongated porphyroclastic clinopyroxene (Fig. 7b). The large and granular orthopyroxenes, plagioclases and secondary clinopyroxenes within the oxide gabbronoritic band retain magmatic textures.

Pargasites in the oxide gabbronoritic band have intermediate compositions between amphibole in the undeformed olivine gabbro and those in the oxide gabbros (Fig. 9). Their Mg# and CaO, TiO_2 and Na_2O contents are slightly lower compared with pargasites in the host mylonitic olivine gabbro. The associated plagioclase and clinopyroxene neoblasts overall display, respectively, more albitic compositions (An = 39-46 and K_2O = 0.11-0.13 wt%; Fig. 10a-b, Fig. 11e, Supplementary Data Table S1) and lower Mg# (~70; Supplementary Data Table S1) compared to plagioclase and clinopyroxene in the host mylonite (Fig. 10, Supplementary Figure S1). The clinopyroxene porphyroclasts display a progressive outward Mg# decrease, from Mg# ~79 at their cores to ~71 in the secondary clinopyroxene (Fig. 10c, Fig. 11f, Supplementary Figure S1). Notably, an overall enrichment in Si, Fe and Na is recorded from the host mylonite to the oxide gabbronoritic band (Fig. 11e-f).

MINERAL TRACE ELEMENT COMPOSITIONS AND AMPHIBOLE OXYGEN ISOTOPES

Undeformed olivine gabbros

Pargasites in undeformed olivine gabbros contain the highest concentrations in compatible trace elements (on average Cr = 870 ppm and V = 1140 ppm; Supplementary Data Table S2) among all amphiboles analysed in this study. They display MORB-type geochemical signature marked by depleted Light Rare Earth Elements (LREE) with respect to Middle REE (MREE)

(La_N/Sm_N = 0.25-0.35; N = C1-chondrite normalized values, after Sun & McDonough, 1989), and nearly flat C1-normalized MREE–Heavy REE (HREE) patterns (Fig. 12a). They show the lowest REE contents (Yb_N = 48 on average) among brown amphiboles from this study (Fig. 12). Overall, pargasite exhibit low Rb and Ba contents, slightly positive Zr-Hf and Nb-Ta anomalies (on average Zr_N/Nd_N = 1.4 and Nb_N/La_N = 1.7) and negative Sr and Eu anomaly ($Eu/Eu^*[Eu_N/\sqrt{(Sm_N * Gd_N)}]$ = 0.6) (Fig. 12b). One sample contains interstitial pargasite with the lowest REE contents (Yb_N = 22), which is comparable to brown amphiboles in other olivine gabbros from Hole U1473A (Fig. 12a). Notably, this pargasite has slightly negative Zr-Hf anomaly (Zr_N/Nd_N = 0.6) and nearly absent Eu anomaly (Eu/Eu* = 0.8) (Fig. 12b).

Associated clinopyroxene and plagioclase have compositions comparable with the data compilation of olivine gabbros from Hole U1473A from other studies (Sanfilippo et al., 2020; Zhang et al., 2020; Boulanger et al., 2021; Ferrando et al., 2021a), showing typical core-rim zonation. Clinopyroxene displays subparallel REE pattern (La_N/Sm_N = 0.08-0.21) compared to those of pargasites at lower concentration levels and exhibits a core-to-rim increase in Y-REE abundances, associated with steepening of Ti, Eu and Sr negative anomalies and flattening of the Zr-Hf anomaly (Fig. 12a-b). Plagioclase overall displays a slight core-to-rim increase in incompatible trace elements, associated with a remarkable LREE enrichment, and a marked positive Ti anomaly (Supplementary Figure S2a-b).

Two samples of undeformed olivine gabbros were selected for oxygen isotope analyses (Fig. 13a; Supplementary Data Table S3). Pargasite from sample 89R-1W, 86-93cm has $\delta^{18}O$ ranging from +4.3‰ to +5.8‰ with an average value of +5.1 ± 0.7‰ (3 grains analysed), whereas pargasite in sample 89R-6W, 4-9cm has $\delta^{18}O$ ranging from +4.7 to +5.5‰ with an average value of +5.0 ± 0.4‰ (4 grains analysed).

Undeformed oxide gabbros and diorites

Pargasitic and edenitic amphiboles in oxide gabbros and diorites have lower compatible trace elements contents compared to those in olivine gabbros (Cr = 6-138 ppm and V = 62-784 ppm; Supplementary Data Table S2). They exhibit trace element patterns subparallel to amphiboles in the olivine gabbros but at higher concentration levels, with edenites being systematically distinct in having the highest REE and Nb-Ta contents (Yb_N = 144-191 in oxide gabbros and Yb_N = 406-590 in diorites; Fig. 12c-d). Strong negative Eu anomalies characterize their

Chondrite-normalized REE patterns (Eu/Eu* = 0.5-0.7 in oxide gabbros and Eu/Eu* = 0.3-0.8 in diorites; Fig. 12c). The extended incompatible trace element patterns exhibit low Rb and Ba contents, prominent negative Sr and Ti anomalies and remarkable Zr-Hf negative anomalies (Zr_N/Nd_N = 0.2-0.4 in oxide gabbro and Zr_N/Nd_N = 0.03-0.6 in diorites; Fig. 12d). Amphiboles from oxide gabbros have the strongest depletion in Nb-Ta (Nb_N/La_N = 0.15 on average), whereas those from diorites show variable but minor Nb-Ta depletion (Nb_N/La_N = 0.91 on average; Fig. 12d). Edenites from diorites display the most marked depletions in LREE relative to MREE (La_N/Sm_N = 0.2-0.3; Fig. 12c) and U-Th (Fig. 12d).

Clinopyroxenes in oxide gabbros are unzoned and exhibit subparallel REE patterns (La_N/Sm_N = 0.16-0.28; Fig. 12c) at higher contents compared to rims of clinopyroxenes from the olivine gabbros. The incompatible element patterns of oxide gabbro clinopyroxenes are markedly depleted in Ti, Zr, Hf and Sr compared to adjacent REE (Fig. 12d). Clinopyroxene in the host gabbro of diorites has trace element compositions comparable with those of clinopyroxene from olivine gabbros, whereas the incompatible element signature of the clinopyroxene rims along the gabbro-diorite contact is similar to that of clinopyroxene from oxide gabbros (Fig. 12c-d).

Plagioclases are unzoned and exhibit subparallel Y-REE patterns at higher contents compared to rims of plagioclase from the olivine gabbros, with plagioclase from diorites having the highest contents (Supplementary Figure S2c). Plagioclase from oxide gabbros has nearly absent Ti anomaly, whereas plagioclase from diorites displays negative Ti anomaly (Supplementary Figure S2d).

The two samples of undeformed diorites, as representative of the most evolved lithology, were selected for oxygen isotope analyses (Fig. 13a; Supplementary Data Table S3). Edenite from sample 39R-4W, 3-8cm have $\delta^{18}O$ ranging from +4.0‰ to +5.2‰ with an average value of +4.6 ±0.6‰ (3 grains analysed), whereas pargasite in sample 89R-3W, 108-110cm have $\delta^{18}O$ ranging from +4.3 to +4.5‰ with an average value of +4.4 ± 0.1‰ (3 grains analysed).

Granulite-facies mylonites

Trace element contents in pargasites from mylonitic olivine gabbros fall in the compositional range defined by pargasites in olivine gabbros (Yb_N = 31-62 and La_N/Sm_N = 0.20-0.35; Fig. 12e-f), although they display compatible trace element contents between those of olivine gabbros and oxide gabbros (Cr = 118-726 ppm and V = 520-1020 ppm; Supplementary Data Table S2). They show absent or slightly negative Eu anomaly (Eu/Eu* = 0.5-0.9) and no to slightly positive Zr-Hf anomaly (Zr_N/Nd_N = 0.9-1.5), whereas the relatively high Nb-Ta contents form a slight positive anomaly (Nb_N/La_N = 0.9-1.8) (Fig. 12f).

Pargasites from the oxide gabbronoritic band display among the lowest contents in compatible trace elements (Cr = 28 ppm and V = 562 ppm; Supplementary Data Table S2). They have higher Y-REE contents (Yb_N = 180 on average) than pargasite in the mylonitic matrix, and slight negative Eu and Zr-Hf anomaly (on average Eu/Eu* = 0.6 and Zr_N/Nd_N = 0.45), as similarly documented for amphibole from oxide gabbros. The incompatible trace element pattern of this REE-rich pargasite exhibits prominent negative Ti and Sr anomalies and lower Nb-Ta contents compared to LREE (Nb_N/La_N = 0.5) (Fig. 12f).

Clinopyroxene and plagioclase porphyroclasts and neoblasts in the mylonitic olivine gabbros have similar compositions, which are comparable with those from the olivine gabbros (clinopyroxene La_N/Sm_N = 0.15-0.25; Fig. 12a-b,e-f; Supplementary Figure S2e-f). Clinopyroxene neoblasts are distinct with negative Ti and Eu anomalies, whereas plagioclase displays no Ti anomaly. In the oxide gabbronoritic band, clinopyroxene porphyroclast have trace element patterns subparallel to those of porphyroclasts in the mylonitic olivine gabbro, but at higher concentration levels, and display prominent negative Ti, Zr-Hf and Sr anomalies (Fig. 12f). Secondary clinopyroxene exhibits trace element patterns subparallel to those of the clinopyroxene porphyroclast, with overall higher concentrations and stronger negative Eu and Ti anomalies (Fig. 12f). Neoblastic plagioclase in the oxide gabbronorite overall displays higher trace element contents (Supplementary Figure S2f).

Pargasites from the two mylonitic olivine gabbros have $\delta^{18}O$ ranging from +5.4 to +6.5‰ (10 grains analysed) in sample 41R-6W, 23-29cm and from +4.7 to +6.1‰ (3 grains analysed) in sample 69R-1W, 23-28cm (the mylonite host was exclusively measured), for an absolute average value of +6.0 ± 0.5‰ (Fig. 13a; Supplementary Data Table S3).

GEOTHERMOMETRIC ESTIMATES

Temperatures of amphibole equilibration in undeformed and deformed rock samples were estimated using amphibole-based geothermometers. We used the amphibole–plagioclase geothermometer (Holland & Blundy, 1994) and the single-amphibole geothermometer (Ti-Fe-

Si-Na in amphibole; Putirka, 2016) assuming a confining pressure of 0.1 GPa. To strengthen our temperature estimates we also applied the recalibration of the Ernst & Liu (1998) Ti-in amphibole geothermometer performed by the Hannover group (Institut für Mineralogie; Leibniz Universität Hannover), which is based on the equation: $-22.1 \times [TiO_2 (wt\%)]^2 + 220.74 \times [TiO_2 (wt\ \%)] + 480.7$. This recalibration has been tested experimentally (France et al., 2010; Koepke et al., 2003) and has been used in several studies (France et al., 2013, 2021; Koepke et al., 2011). The plagioclase-amphibole geothermometer was applied to adjacent amphibole-plagioclase rim pairs in undeformed lithologies, whereas we selected neoblastic amphibole-plagioclase aggregates for temperature estimates of the ductile deformation in mylonites. The single-amphibole geothermometers yield overall comparable equilibrium temperature values (Fig. 13b), providing rather broad temperature ranges that reflect the wide Ti variations in the analysed amphiboles (see Fig. 9), whereas the amphibole–plagioclase geothermometer yield slightly lower equilibrium temperatures.

For comparison, clinopyroxene-plagioclase equilibrium temperatures were determined for adjacent crystal rim couples identified in undeformed olivine gabbros and oxide gabbros and displaying equilibrium magmatic textures. We applied the geothermometer from Sun et al. (2017) based on partitioning of REE between the two minerals, estimating 1070-1100°C for olivine gabbros and 970-990°C for oxide gabbros. Considering the ~50°C intrinsic error of the clinopyroxene-plagioclase geothermometer, the results are slightly higher, but comparable with the temperature estimates obtained from amphiboles and amphibole-plagioclase pairs compositions. It should be noted that clinopyroxene-plagioclase temperature estimates obtained from olivine gabbros are ~100°C higher compared with temperature values from amphiboles. Probably, due to the large laser ablation spot-size (see *Chemical maps and in situ analyses*), the trace elements measurements of clinopyroxene were not exclusively performed at the outermost crystal rim in equilibrium with amphibole, but instead could represent a mixed analysis with a component of a slightly more internal and less chemically evolved area of the clinopyroxene crystal.

The highest temperature estimates obtained from all four geothermometers (i.e., using amphibole, plagioclase and clinopyroxene compositions) are recorded by the olivine gabbros, with averages of ~890°C for amphibole-plagioclase pairs, averages ranging from 925 to 940°C for single-amphiboles (all data fall within the interval 850-1010°C), and ~1100°C for clinopyroxene-plagioclase pairs (Fig. 13b). Oxide gabbros record slightly lower crystallization temperatures ranging from 825 to 870°C (averages) for amphibole-plagioclase pairs, between

850 and 940°C (averages; all data fall in the interval 805-990°C) for single-amphiboles, and ~980°C on average for clinopyroxene-plagioclase pairs. The lowest temperatures were determined for diorites yielding averages of ~810°C for amphibole-plagioclase pairs and 780-925°C for single-amphiboles (Fig. 13b).

Temperature estimates for the dynamic recrystallization event under granulite-facies conditions fall within the interval of temperatures obtained for undeformed olivine gabbro, with averages of ~870°C for amphibole-plagioclase pairs and ranging within the interval 870-955°C for single-amphiboles (Fig. 13b). In particular, the amphiboles from the oxide gabbronoritic band show on average slightly lower, although partly overlapping, equilibrium temperatures compared with the granulite-facies mylonite (amphibole-plagioclase pair $T_{average}$ = 840°C; single-amphiboles $T_{average}$ = 865-900°C).

DISCUSSION

Magmatic formation of brown amphiboles

Throughout the lower oceanic crust recovered at Hole U1473A, brown amphibole appears in chemically distinct gabbroic rocks and in various textural occurrences. In undeformed samples, pargasites form interstitial films locally mantling the grain boundaries of primary mineral phases in primitive olivine gabbros (Fig. 4c) and, locally, in oxide gabbros (Fig. 4f), whereas edenites are larger interstitial grains in the most evolved oxide gabbros (Fig. 4g) and subhedral to poikilitic crystals in diorites (Fig. 5a). Pargasitic amphibole in mylonites forms fine-grained assemblages with polygonal morphology (Fig. 6c) or occurs as anhedral single crystals at grain boundaries of porphyroclastic clinopyroxene (Fig. 6e). The textures of all brown amphiboles from this study attest of their textural equilibrium with the primary mineral phases (i.e., olivine, plagioclase and clinopyroxene) or with the neoblastic mineral assemblage. These textural relationships contrast with the characteristics of hydrothermal brown amphiboles commonly described as coronas with irregular grain boundaries around or completely replacing primary clinopyroxene, and in crosscutting monomineralic amphibole veins (e.g., Coogan et al., 2001; Gillis & Meyer, 2001; Miranda & John, 2010; Gaggero & Cortesogno, 1997; MacLeod et l., 2017).

The high-Ti contents yielding high equilibrium temperatures of the studied amphiboles (up to ~1000°C in olivine gabbros) are comparable with magmatic amphiboles from other oceanic crustal sections, and contrast with the low-Ti content of the hydrothermal amphiboles (Fig. 14a). Such high equilibrium temperatures, together with equilibrium textures point to crystallization of brown amphiboles from hydrous melts (e.g., Coogan et al., 2001). The association of pargasites and edenites with Fe-Ti oxide phases and with other late-stage cumulus phases (i.e., apatite and zircon) strongly supports the magmatic nature of brown amphiboles in all studied samples. Furthermore, Ti, Al, Y-REEs, Zr-Hf and Nb contents in amphiboles are systematically higher than associated clinopyroxene (Figs. 12, 14a), all showing trace element subparallel patterns and comparable LREE/HREE ratios (Fig. 14b). These geochemical characteristics thereby point to a common parental melt of clinopyroxene and adjacent amphibole in further agreement with a magmatic origin.

In addition, bleb-shaped amphiboles occur within cores of large cumulus clinopyroxene crystals in U1473A undeformed olivine gabbros and oxide gabbros. Similar amphibole textural occurrences have been observed in samples from other oceanic spreading centres (e.g., MARK area and Atlantis Bank OCC [Coogan et al., 2001; Lissenberg & MacLeod, 2016] and Parece Vela Basin [Harigane et al., 2019]) and were interpreted as resulting from melt-mineral interaction triggered by ingress of hydrous evolved magmatic fluids into the clinopyroxene crystal (e.g., Lissenberg & MacLeod, 2016). Likewise, the elongated shape of the studied bleb amphiboles oriented parallel to the clinopyroxene cleavage planes is consistent with the mechanism of melt infiltration into the cumulus crystal along its crystalline weak planes (intracrystalline melt migration, e.g., Basch et al., 2021), thereby corroborating the magmatic origin of the brown amphiboles.

Origin of the hydrous component

Seawater components contain high Cl and LREE compared to tholeitic melts thereby causing the precipitation of brown amphiboles typically with Cl >0.15 wt% and $La_N/Sm_N > 0.4$, and low abundances of fluid-immobile elements as Nb (e.g., Cortesogno et al., 2000; Coogan et al., 2001; Gillis & Meyer, 2001; Harigane et al., 2019). The remarkably low Cl contents and rather low LREE/HREE ($La_N/Sm_N < 0.5$; Fig. 14b), the slightly positive Nb anomalies (Fig. 12b,d,f) and the depletion in fluid mobile elements such as Rb and Ba (e.g., Klinkhammer et al., 1994) in amphiboles from this study point to a first order negligible seawater components in their parental melts.

The $\delta^{18}O$ values are one of the most powerful tracers of seawater in hydrous melts, which typically lead to ^{18}O-depletion during high temperature hydrothermal alteration and strong ^{18}O-enrichments during low temperature alteration processes and weathering (e.g., Gregory & Taylor, 1981; Stake, 1991; Alt & Bach, 2006). The $\delta^{18}O$ values of amphiboles from this study are much higher than the $\delta^{18}O$ of hydrothermal hornblendes in the Atlantis Bank crustal section ($\delta^{18}O < +2.0‰$; Stakes, 1991; Alt & Bach, 2006; Fig. 13a). Despite this, our data reveal a certain extent of variability in $\delta^{18}O$ that ranges from +4.4‰ in diorite veins to +6.1‰ in mylonites (averages; Fig. 13a). This variability can be related to magmatic processes, as oxygen isotopes fractionation can be caused by differential uptakes of O isotopes between minerals and melts, as governed by a fractionation factor ($\Delta_{mineral-melt}$). To account for differences in $\Delta_{mineral-melt}$ of each crystallized mineral (see Fig. 15), we calculated melts in equilibrium with amphiboles (this study), olivine and clinopyroxene from the Atlantis Bank lower oceanic crust (Gao et al., 2006; Pietranik et al., 2017; Fig. 15). Remarkably, the oxygen isotopic compositions of melts in equilibrium with pargasites (both undeformed and mylonitic gabbros), olivine, clinopyroxene and plagioclase fall within the same compositional field, having $\delta^{18}O$ ranging between +5.0‰ and +6.5‰. This $\delta^{18}O$ interval encompasses the $\delta^{18}O$ values of erupted MORB, in further agreement with the magmatic character of the hydrous component in the amphibole parental melt. We note that the mylonitic olivine gabbros contain pargasites slightly ^{18}O-enriched respect to pargasites in undeformed samples (Fig. 13a); this possibly suggests the involvement of a more differentiated melt during the deformation event, given that fractionation generally causes uptake of ^{16}O in early crystallized minerals (i.e., olivine and clinopyroxene). Indeed, fractional crystallization models of tholeiitic melts (Bucholz et al., 2017) predict progressive ^{18}O enrichments of the differentiating melt, caused by the crystallization of a mineral assemblage dominated by olivine, clinopyroxene and plagioclase.

Although $\delta^{18}O$ values of melts in equilibrium with olivine, plagioclase, clinopyroxene and zircon comply with a fractional crystallization trend (Fig. 15), we note a remarkable decrease in $\delta^{18}O$ (down to +4.4‰, sample average value; Fig. 13a) in brown amphibole from the most chemically evolved diorites that is inconsistent with simple magmatic differentiation. Similar ^{18}O-depleted compositions have been reported for amphiboles in felsic dikes and amphibole-rich gabbros from the Ligurian Ophiolites (Tribuzio et al., 2014). Based on the oxygen isotope compositions of coexisting zircons and clinopyroxene, these felsic veins were interpreted of magmatic origin and the unexpectedly low $\delta^{18}O$ values could reflect oxygen isotope exchange during slow cooling (Tribuzio et al., 2014). In the case U1473A diorite veins, the abundant plagioclase (~40 vol%) could have acted as host of ^{18}O, resulting in a progressive decrease of $\delta^{18}O$ in magmatic edenites. However, equilibrium temperatures estimated from Ti contents in these amphiboles are consistent with magmatic crystallization of a differentiated melt and do not strictly point to cooling. Alternatively, ^{18}O depletion in diorite amphiboles can possibly be the effect of assimilation of a hydrothermally altered rock during magmatic crystallization. We run a model of assimilation-fractional crystallization process (AFC; DePaolo et al., 1981) assuming as assimilation of a hydrthermally altered oceanic crust ($\delta^{18}O = 3$; from Stakes, 1991; Alt & Bach, 2006) and as starting composition a melt in isotopic equilibrium with average $\delta^{18}O$ values of pargasites in undeformed olivine gabbros. We tested different ratios of crystallized/assimilated masses, ranging from 1.5 to 2.5; the $\delta^{18}O$ values of edenites in diorite veins are best reproduced by the crystallized/assimilated ratio of 2 (see Fig. 15 for details on the model parameters). Despite no clear evidence seawater-derived features in major and trace element compositions of amphiboles, the high susceptibility of oxygen isotopes makes them unique tracers of seawater components. Thus, the $\delta^{18}O$ values of edenites reveal that diorites emplaced after the ingress of hydrothermal fluids in the gabbros.

To summarize, oxygen isotopes and mineral chemistry of undeformed and mylonitic olivine gabbros indicate that the hydrous component in the parental melts is not seawater related but of magmatic origin. On the other hand, the oxygen isotopic composition of amphibole in diorite veins suggests a possible involvement of hydrothermal minerals assimilation during the progressive magmatic crystallization of the differentiated melts.

Evolution of late-stage melts

Calculated REE_{Amp}/REE_{Cpx} ratios between brown amphibole and adjacent clinopyroxene crystal rim or between adjacent neoblasts produce nearly flat REE patterns in undeformed and mylonitic olivine gabbros and oxide gabbros (Supplementary Figure S3; exception of diorite veins is treated in '*Diorites as frozen late-stage melts that locally hybridized the host gabbro*'). These clinopyroxene-amphibole correlations suggest that the brown amphibole and clinopyroxene rims crystallized from a common melt, which was chemically distinct in each lithology.

Clinopyroxene and amphibole fall along the same TiO_2-Al_2O_3 trend (Fig. 14a), displaying a progressive decrease in Mg#, Al_2O_3 and CaO (Figs. 9, S1) and concomitant increase in Y-REE (Fig. 12a,c) from the olivine gabbros to the oxide gabbros, with mylonites showing similar compositions to olivine gabbros. Because decreasing Ca and Mg at increasing REEs in the melt typically result from magmatic crystallization (e.g., Grove et al., 1992), the chemical compositions of the mineral phases are directly representative of the differentiation stage of the parental melt. The chemically evolved signature of edenites in oxide gabbros and diorites, and their association with apatite and minor zircons, suggest that their parental melts experienced higher extents of magmatic differentiation compared with the primitive parental melts of olivine gabbros. Surprisingly, in each lithology, the significant variations in amphibole TiO_2 defining parallel Ti-Mg# negative correlations (Fig. 9) seem inconsistent with a typical magmatic crystallization trend of primitive MORB (e.g., Villiger et al., 2007; Husen et al., 2016). In oxide gabbros, the edenitic (lower Ti) amphibole shows the highest Mg# compared to the pargasitic (higher Ti) counterpart. This is coherent with crystallization of Fe-Ti oxide phases that deplete the melt preferentially in FeO and TiO_2, concomitantly with the precipitation of Fe-depleted edenites. This process occurred during the closure of the system permeability within each lithological group. In the following, we reconstruct the magmatic formation of brown amphibole throughout the crustal section sampled in Hole U1473A at the Atlantis Bank OCC.

To unravel the evolution of melts crystallizing brown amphiboles throughout the Atlantis Bank lower oceanic crust, we calculated the major and trace element compositions of melts in equilibrium with both amphiboles and adjacent clinopyroxene rims. Melt silica contents were determined from amphibole compositions applying the equation (10) in Putirka (2016), whereas Ti and Fe-Mg concentrations were calculated using partition coefficients (K_d) from Nandedkar et al. (2016) and Tiepolo et al. (2007) for amphiboles and from Villiger et al. (2007) for clinopyroxenes (see details in Fig. 16a). Concentrations of REEs in equilibrium melts were determined using REE K_ds calculated from LA-ICP-MS measurements of amphiboles and clinopyroxene rims applying the 'mineral-based model' by Shimizu et al. (2017) and the lattice strain model by Sun & Liang (2011), respectively. ${}^{Amp/melt}K_d$ and ${}^{Cpx/melt}K_d$ were calibrated at the temperatures estimated with amphibole and clinopyroxene-plagioclase geothermometers (see section '*Geothermometric estimates*').

Origin of pargasite in olivine gabbros

Comparing the compositions of primary minerals from the Atlantis Bank lower oceanic crust (Dick et al., 2002) with the experimentally reproduced chemical evolution of MORB-type melts (Feig et al., 2006, 2010), Feig et al. (2010) inferred that the gabbroic rocks from the SWIR crystallized from MORBs having low water contents and under reducing conditions. Nevertheless, hydrous conditions are a fundamental prerequisite for amphibole crystallization (e.g., Johnson et al., 1994; Merzbacher & Eggler, 1984). Assuming water contents in pargasite ~1.1 wt% (the lowest H_2O contents measured in chemically comparable magmatic amphibole from Tribuzio et al., 2000; see Fig. 14a) and if $^{Amp/melt}K_d$ of H_2O is 0.3 (Tiepolo, 1999; Hauri et al., 2006), the water content of interstitial melts should have reached ~3.7wt% at the time of amphibole crystallization in the studied olivine gabbros.

At low melt fractions, the water content in MORB increases rapidly as advanced melt differentiation proceeds, due to crystallization of anhydrous crystals (i.e., olivine, plagioclase and clinopyroxene; Koepke et al., 2018). Within the lower oceanic crust at the Atlantis Bank OCC, saturation of interstitial brown amphibole in olivine gabbros has been estimated after ~90-95% of melt crystallization (Gillis & Meyer, 2001). We modelled fractional crystallization of a primitive N-MORB from the study area (Mg#~62; Coogan et al., 2004), using MELTS (Ghiorso & Sack, 1995) at ~0.1-0.2 GPa pressure conditions, and estimate that such advanced melt fractionation can be reached at ~980°C (5% remaining melt fraction). Notably, these temperatures approximate the ~1000°C equilibrium temperatures estimated for crystallization of pargasite and rims of cumulus minerals (average between all geothermometers; Fig. 13b) in the U1473A olivine gabbros, hence well reconciling with a process of extreme crystallization of MORB-type melts. In other words, interstitial pargasite in undeformed olivine gabbros likely crystallized from a melt trapped in the crystal matrix during the latest stages of melt differentiation (see also Gillis & Meyer, 2001). We infer that the stability of hydrous conditions was achieved after crystallization of more than 95 vol% of the melt mass, consistent with the occurrence of Fe-Ti oxides in textural equilibrium with the pargasite (Fig. 4c) and MELTS computations.

Amphibole crystallization from trapped late-stage melts is also consistent with major and trace element compositions of melts in equilibrium with the interstitial pargasites and clinopyroxene rims. Major element compositions of such equilibrium lay within the experimentally determined line of descent of a MORB at low pressure conditions (0.1 GPa; Husen et al., 2016; Fig. 16a). Taking into account the ~4 wt% intrinsic error of the Putirka (2016) equation, the computed average ~64 wt% of SiO_2 content in the equilibrium melts is comparable with the experimentally acquired melts coexisting with olivine + plagioclase + clinopyroxene (i.e., typical paragenesis of olivine gabbros) + amphibole + Fe-Ti oxides (SiO_2 ~59 wt% from Feig et al., 2006). Yet, the estimated REE concentrations in the equilibrium melt of pargasite (Supplementary Figure S4a,b) and clinopyroxene rims (Supplementary Figure S4c,d) fall in the REE compositional field of MORBs (Supplementary Figure S4e), although slight enrichments in the most incompatible LREE characterize characterize all REE patterns of the calculated equilibrium melts (Supplementary Figure S4e). Enrichments in the most incompatible elements (Zr, Hf, LREE) compared to less incompatible elements (M-HREE, Y) at the rims of clinopyroxene and plagioclase crystals have been documented in olivine gabbros from the Atlantis Bank OCC (Boulanger et al., 2020, 2021; Gao et al., 2007; Lissenberg & MacLeod, 2016; Sanfilippo et al., 2020; Zhang et al., 2020; Ferrando et al., 2021a), and are commonly interpreted as resulting from reactive melt percolation or subsolidus diffusion (Coogan & O'Hara, 2015). In the first scenario, this melt migration might have occurred within a high-porosity crystal mush (>50% of melt fraction; Ferrando et al., 2021a,b) and triggered assimilation of the pre-existing gabbroic minerals, and concomitant crystallization of new phases. The cores of cumulus phases preserved their primary compositions, whereas crystal rims record the composition of the migrating melt (see Sanfilippo et al., 2020; Ferrando et al., 2021a). In the second scenario, fractional crystallization of interstitial melt caused the increase in incompatible trace elements, later followed by subsolidus diffusion between coexisting plagioclase and clinopyroxene (Coogan & O'Hara, 2015). We do not want to discuss the origin of the chemical zoning here. However, we note that the chemical equilibrium between clinopyroxene rims and associated interstitial pargasites (Supplementary Figure S3) indicate that both mineral phases precipitated from a melt having inherent enrichments in highly incompatible trace elements. This leads us to preferably interpret the incompatible trace element compositions of the amphibole and co-existing clinopyroxene rims as record of late-stage hydrous melt.

In summary, pargasite in undeformed olivine gabbros crystallized from late-stage chemically evolved melts residual after crystal mush-melt interactions. The equilibrium textures of brown amphiboles indicate that the reactive process stopped prior to pargasite precipitation. Crystallization of interstitial pargasite proceeded in chemical equilibrium with the clinopyroxene rims (Supplementary Figure S3). The wide variations in single-amphibole equilibrium temperatures suggest that amphibole crystallization occurred at decreasing temperature during the closure of the system, as also evidenced by their interstitial textural occurrence. Additionally, the magmatic late-stage origin of interstitial pargasites is supported by their local association with Fe-Ti oxide phases, interstitial orthopyroxene and apatite, a mineral assemblage that experimentally stabilizes in the latest stages of MORBs magmatic crystallization processes (T<1050°C; Berndt et al., 2005; Feig et al., 2006).

Origin of the oxide gabbros

Oxide gabbros from the Atlantis Bank lower oceanic crust are considered to represent cumulates or mixtures of cumulates and frozen melts, based on their low SiO_2 content compared to true residual melts (Robinson et al., 1991; Natland et al., 1991; Dick et al., 1999, 2000). Accordingly, they are characterized by the lowest An contents of plagioclase and the lowest Mg# of clinopyroxene among the gabbroic rocks (Figs. 10, S1) and record lower equilibrium temperature compared to olivine gabbros (Fig. 13b).

During magmatic differentiation at low pressure conditions, a MORB-type melt typically displays an early increase in Ti and Fe, ultimately leading to saturation of Fe-Ti oxide phases (e.g., Toplis & Carroll, 1995; Berndt et al., 2005; Botcharnikov et al., 2008). In turn, the subsequent crystallization of Fe-Ti oxides causes progressive loss of Ti, Fe, along with other strongly compatible, as Cr and V (e.g., Irving, 1978; Righter et al., 2006), and HFSE (i.e., Zr, Hf, Nb, and Ta; e.g., Klemme et al., 2006), coupled with increase in strongly incompatible trace elements U, Th and Y-REE (e.g., Klemme et al., 2006) in the residual melt. Consistently, amphiboles in the studied oxide gabbros display lower V and HFSE and higher Y-REE contents at nearly constant Sc (moderately compatible in Fe-Ti oxides; e.g., Klemme et al., 2006) compared to the olivine gabbros (Fig. 12a,c, Fig.16a). Hence, the synchronous crystallization of Ti-Fe oxides and plagioclase, delineate the oxide-bearing lithologies in the V/Sc, Sr/Nd and V/Y spaces (Fig. 17). In particular, the accumulation of up to 5 vol% Fe-Ti oxides within the oxide gabbros (Fig. 4f,g) causes lower V/Sc, Sr/Nd and V/Y but higher Y compared to the olivine gabbros, where the accumulation of less than 0.5 vol% of Fe-Ti oxides shows an extremely local effect on the residual melt composition.

The iron contents of computed melts in equilibrium with amphibole and clinopyroxene from the U1473A oxide gabbros are comparable with typical compositions of ferrobasalts (e.g., le Roex et al., 1982; Das et al., 2012; Fig. 16a), as well as their HREE contents (see comparison with oceanic ferrobasalts in Fig. 16b). The ferrobasaltic affinity of the equilibrium melts is, however, in contrast with their substantially low TiO_2 concentrations (Fig. 16a). This discrepancy could derive from crystallization of Fe-Ti oxide phases, the major host of Ti, prior to amphibole precipitation. This is in line with the interstitial habit of amphiboles occurring between euhedral to subhedral crystals of plagioclase, clinopyroxene and Fe-Ti oxides, and is also consistent with laboratory experiments that predict crystallization of clinopyroxene + Fe-Ti oxides as liquidus assemblage of a ferrobasaltic melt (melt composition: SiO_2 = 49.5 wt%, TiO_2 = 3.7 wt%, FeO = 17.9 wt%; Koepke et al., 2018; Fig. 16a). Koepke et al. (2018), simulating a late-stage MORB system, demonstrated that the mineral assemblage composed of Fe-Ti oxides + clinopyroxene + plagioclase forms between 1000°C and 900°C, wilth apatite appearing on the liquidus at ~950°C and amphibole at temperatures of <900°C. Our temperature estimates of clinopyroxene-plagioclase (~980°C on average) and amphibole (~900°C on average) crystallization in U1473A oxide gabbros approximately agree with these experimental reationships. Moreover, the occurrence of late-stage highly differentiated phases (e.g., the large euhedral apatite crystals in association with edenites in an oxide gabbro) point to apatite saturation prior to precipitation of edenites, as predicted by the crystallization experiments (Fig. 16a). Hence, the mineral textural relationships in U1473A oxide gabbros and the compositions of their equilibrium melts are compatible with a process of extreme melt chemical evolution.

Diorites as frozen melts that locally hybridized the host gabbro

Diorite veins, together with quartz-diorites, tonalites and trondhjemites (collectively termed “oceanic plagiogranites”, see Koepke et al. 2007) are ubiquitous features in sections of slow-spreading lower oceanic crust (e.g., Coleman & Donato, 1979; Blackman et al., 2006; MacLeod et al., 2017). Despite the consensus that oceanic plagiogranites formed by crystallization of SiO_2-enriched melts carrying high concentrations of incompatible elements, the origin of such highly differentiated melts is strongly debated. These felsic melts are interpreted either as products of gabbro partial melting triggered by ingress of seawater-rich fluids (e.g., Dick, et al., 1991; Koepke et al., 2004, 2007) or as late-stage differentiates of MORB-type melts (e.g., Niu et al., 2002; Berndt et al., 2005; Feig et al., 2006; Nguyen et al., 2018; Chen et al., 2019; Ma et al., 2020). In the case of edenites from the studied diorite veins, their chemical compositions, including trace element contents, are comparable with amphiboles in other felsic veins from the Atlantis Bank lower oceanic crust (Figs. 9, 14a) mostly interpreted as products of 85% to 90% fractionation of a primitive MORB (Niu et al., 2002; Nguyen et al., 2018; Type I in Ma et al., 2020). In detail, the marked Zr-Hf negative anomalies (Fig. 12d) and the extremely low V/Sc (Fig. 17a) and Sr/Nd ratios (Fig. 17b) at high incompatible trace element contents in diorite edenites is consistent with a process of advanced crystallization of a MORB-type melt (e.g., Coleman & Donato, 1979; Floyd et al. 1998; Beccaluva et al. 1999; Niu et al. 2002), thereby resulting in a SiO_2 enrichment in the residual melt. The high SiO_2 contents in the calculated melts in equilibrium with the edenites (SiO_2 on average ~74 ±4 wt%) are also in agreement with the hypothesis that highly differentiated MORB formed some of the U1473A diorite veins (Fig. 16b, S4). The evolved nature of the melt promoted the crystallization of chemically zoned Na-rich plagioclase, from core (An ~35) to rim progressively more enriched in the albitic component (An <20).

Edenites from the studied diorite veins and their calculated equilibrium melts (Fig. 16b, S4) have the most evolved chemical compositions, having REE patterns parallel to those of pargasites in olivine gabbros and oxide gabbros, and locally overlapping the edenites from the oxide gabbros (Figs. 9, 12a-d, 14c). These chemical relationships suggest that the parental melts of diorite veins and that of brown amphibole in the oxide gabbros might have been genetically related. In the previous section, we have documented that Si-rich melts residual from crystallization of the olivine gabbros could have been extracted to form the oxide gabbros. The lower TiO_2 Al_2O_3 and Zr-Hf of the diorite indicate that precipitation of Fe-Ti oxide phases occurred before the formation of these felsic veins, likely accumulated in the discrete levels of oxide gabbros. The melt residual from the formation of the ox-gabbros could have been partially extracted to ultimately form the diorite veins.

The sharp contacts (Fig. 5a) between the diorite veins and the host gabbro, the crosscutting relationship and the low ^{18}O isotopes in the dioritic amphibole concur that felsic vein emplacement occurred during the cooling of the lower crustal section, and likely followed the high temperature hydrothermal alteration of the sequence. Indeed, the computed equilibrium temperatures of edenites in diorites range from values as low as ~750°C, in agreement with estimated solidus temperatures of a late-stage MORB under water-saturated conditions (~800°C; Koepke et al., 2018), to slightly higher values than temperature estimates for brown amphibole crystallization in oxide gabbros (T ~900-950°C; Fig. 13b).

Hence, the diorite veins do not exclusively represent crystallized and frozen *in-situ* residual late-stage MORB-type melts. The oxygen isotopic composition of brown amphibole seems to record minor seawater component in the parental melt, possibly related to partial assimilation of hydrothermal minerals (Fig. 15). Such hydrothermal minerals may be present in a local crosscutting vein, or within gabbros encountered by the melt during its migration throughout the crust prior to diorite vein formation. Moreover, at the diorite-host gabbro contact, the coronitic edenite on rims of clinopyroxene from the host gabbro (Fig. 5b) attest disequilibrium between the two lithologies. The host rock shows strong Fe and Y-REE enrichments at the clinopyroxene rims (Fig. S1, Fig. 12c,d) and progressively Na-rich plagioclases (comparable with plagioclase in the diorite vein core; Fig. 10a), approaching the felsic vein, hence indicating a diffuse chemical contact. The clinopyroxene rim and coronitic edenites are in chemical disequilibrium (Supplementary Figure S3). These chemical and textural features suggest that the melt crystallizing the felsic material reacted with the host gabbro, which was locally hybridized along the contact (see also Basch et al., 2020). During the reaction and final local re-equilibration of the host gabbro with the felsic material, compatible elements were buffered by the host rock leading to unexpectedly high Mg contents in the newly formed melt (Fig. 16a).

Crystal plastic deformation in presence of melt: interstitial or externally derived melts?

Plastic deformation of the Atlantis Bank lower oceanic crust is widespread and occurs predominantly in the uppermost part of the massif (first 500–600 m) before being more heterogeneous and localized down section (Dick et al., 2019a). Strain localization in shear zones developed during the progressive crustal exhumation and formation of the Oceanic Core Complex (e.g., Miranda & John, 2010). Initiation of detachment faulting was proposed to be coeval with magma crystallization under hypersolidus conditions based on the presence of magmatic fabrics overprinted by subparallel granulite-facies crystal plastic fabrics (e.g., Cannat, 1991; Cannat et al., 1991; Dick et al., 1991; Dick et al., 2000). The local occurrence of oxide-rich lithologies in shear zones further suggests the onset of deformation in the presence of melt (e.g., Bloomer et al., 1991; Dick et al., 2000; Natland & Dick, 2001), favoring transport of late-stage differentiated melts (e.g., Zhang et al., 2020). The common occurrence of thick granulite-facies shear zones in olivine gabbros with no obvious involvement of a melt phase (i.e., lack of oxide-rich intervals) was interpreted to attest the development of high-temperature plastic deformation under solid-state conditions (Miranda & John, 2010). However, the local presence of amphiboles and late-stage differentiated mineral phases in a fine-grained recrystallized matrix suggests melt infiltration also in solid mylonites. Continuous dynamic recrystallization and grain-size reduction created higher porosity pathways for melt percolation (Mehl & Hirth, 2008; Taufner et al., 2020), in turn leading to significant local rheological weakening associated with enhanced melt ingress along grain boundaries. The presence of melt would then favour strain localization (Sanfilippo et al., 2019; Gardner et al., 2020; Casini et al., 2021).

The widely documented microstructural evidence of both syn-magmatic deformation (e.g., Bloomer et al., 1991; Dick et al., 2000; Natland & Dick, 2001) and solid-state deformation coupled with the positive feedback between rheological weakening and melt percolation (e.g., Mehl & Hirth, 2008; Miranda & John, 2010; Gardner et al., 2020) imply distinct melt sources. The former involves late-stage differentiated melts residual from magmatic crystallization of the gabbroic sequence, whereas the latter assumes migration of melts in chemical disequilibrium with the host gabbro. The distinct microstructural and chemical characteristics of the granulite-facies mylonites selected for this study document these different stages of plastic deformation, elucidating the main differences between deformation in a closed system and melt-assisted deformation in an open system.

Deformation of a melt-bearing olivine gabbro

The foliation of the mylonitic olivine gabbro 41R-6W, 23-29 (hereafter referred to as 41-6) is defined by elongated porphyroclastic olivine and clinopyroxene crystals, and minor relicts of plagioclase, mantled by the neoblastic assemblage of pyroxenes + pargasite + Fe-Ti oxide phases + apatite alternating with bands of neoblastic plagioclase (Fig. 6). Chemical composition of porphyroclastic and neoblastic clinopyroxenes and plagioclases overlap with compositions of clinopyroxene and plagioclase crystals in undeformed olivine gabbros, covering the whole compositional range from more primitive crystal cores to more evolved crystal rims (Fig. 10, Fig. 11, Fig. 12, Supplementary Figure S1). The close chemical relationship between plastically deformed and undeformed olivine gabbros, together with internal deformation of porphyroclastic minerals, suggest that a similar agent was involved during high-temperature crystal-plastic deformation. Dislocation creep dominated concomitantly with dynamic recrystallization that resulted in the formation of neoblastic grains with little internal deformation (e.g., Mehl & Hirth, 2008; Miranda & John, 2010).

Pargasitic amphiboles occurring between neoblastic clinopyroxene (Fig. 6a-b) have compositions that also coincide with those of interstitial pargasite in undeformed olivine gabbros (Figs. 9, 12). Notably, neoblastic clinopyroxene associated with pargasite is Fe-rich, similar to clinopyroxene rims in the undeformed rock. In addition, pargasite forms few tens of µm-thick bands in association with Fe-Ti oxide and apatite, a mineral assemblage typically observed along grain boundaries of the primary minerals in undeformed olivine gabbro (Fig. 4c). We argued that precipitation of interstitial pargasite in undeformed olivine gabbro is the result of late-stage crystallization of the residual differentiated MORB-type melt entrapped within the crystal matrix (see '*Origin of pargasite in olivine gabbros*'). Similarly, the high TiO_2 contents and the low Cl and LILE contents together with low LREE/HREE ratios in pargasites from mylonitic olivine gabbros are consistent with precipitation of brown amphibole from residual melts after advanced magmatic differentiation, trapped interstitially within the olivine gabbro.

However, mineral chemistry alone does not allow to unravel the timing of pargasite precipitation within the mylonitic olivine gabbro; pargasite could either have precipitated previously from the melt and recrystallized during the plastic deformation event, or crystallized from the trapped melt during deformation. If pargasite in the studied mylonite formed by high-temperature recrystallization of a solid olivine gabbro containing interstitial brown amphibole, then pargasite should exclusively occur as equigranular polygonal grains. Despite the local occurrence of such neoblastic textures, pargasite commonly also appears as 500 µm-stretched anhedral grains at the contact with clinopyroxene porphyroclasts (Fig. 6e). This suggests that melt was still present interstitially in the olivine gabbro during the initiation of the plastic deformation event. Hence, we attribute the pargasite in the mylonitic olivine gabbro to precipitation of interstitial melts, residual from prior crystallization of the olivine gabbro mineral assemblage, during deformation. In this scenario, plastic deformation initiated in a melt-bearing olivine gabbro, consistent with the high equilibrium temperatures computed from the pargasitic amphiboles chemistry (870-955°C; Fig. 13b) and in line with the hypothesis that detachment faulting is rooted into partially molten crystal mushes (e.g., Bloomer et al., 1991; Dick et al., 2000; Natland & Dick, 2001).

Melt flow in a deformed olivine gabbro

The mylonitic olivine gabbro in sample 69R-1W, 23-28cm (hereafter referred to as 69-1) shares similar textural and mineral chemical features with the other mylonite from this study. The neoblastic assemblage of pyroxenes + pargasite + Fe-Ti oxide phases + apatite mantles elongated porphyroclastic olivine, clinopyroxene and plagioclase crystals, and alternates with bands of neoblastic plagioclase (Fig. 7). Additionally, the mineral compositions of the mylonite overlap with those of the other mylonitic sample and the undeformed olivine gabbros (Fig. 9, Fig. 10, Fig. 12), suggesting that plastic deformation likely initially developed in a melt-bearing olivine gabbro (see previous section). Yet, sample 69-1 is characterized by remarkably stronger grain size heterogeneity than that in the mylonitic sample 41-6 (Fig. 7 vs Fig. 6, respectively), with alternating bands of large preserved porphyroclasts and bands of parallelly oriented fully recrystallized fine (~100 µm) to very fine (~50µm) neoblastic assemblage. Notably, the computed equilibrium temperatures (Fig. 13b) from pargasite in mylonite 69-1 are on average ~40°C lower than in the mylonite 41-6. Thus, this possibly suggests that strain was further localized in the very fine-grained recrystallized bands at decreasing temperatures (e.g., Etheridge & Wilkie, 1979; Jaroslow et al., 1996).

The crosscutting oxide gabbronoritic band slightly deflects the crystal-plastic fabric of the 69-1 mylonitic olivine gabbro shows unambiguous magmatic textures that contrast with the mylonitic recrystallization of the host rock. Within the core of this band, secondary clinopyroxene overgrown on pre-existing porphyroclastic clinopyroxene displays strong Fe enrichment (Supplementary Figure S1) and has overall high incompatible trace element contents (Fig. 12e,f). Secondary clinopyroxene is associated with euhedral mm-size orthopyroxene, abundant undeformed apatite and Fe-Ti oxide phases (Fig. 7b), and chemically evolved Na-rich plagioclase (Fig. 10, Supplementary Figure S2) forming subhedral to locally interstitial grains of few hundred-µm size (Fig. 7d). Pargasite is mostly concentrated along the contact with the host rock in association with neoblasts of pyroxenes and plagioclase, and displays lower Mg# and CaO (Fig. 9) and overall higher incompatible trace elements (Fig. 12e,f) respect to pargasite in the host mylonite. In addition, within the pargasite-rich level, a euhedral mm-size titanite is characterized by well-developed grain boundaries (Fig. 7a,b); its size and shape, together with the lack of obvious textures of metamorphic substitution, suggest a magmatic origin of the titanite crystal (see Kohn, 2017 and references therein). Strikingly, the development of pargasite + titanite phase association occurs away from the Fe-Ti oxide-rich level in the core of the oxide gabbronoritic band where pargasite is absent. This points to titanite formation from a chemically evolved melt under high water activity conditions at the expense of ilmenite (e.g., Xirouchakis et al., 2001), likely as the result of a simultaneous increase in oxygen fugacity (e.g., Frost et al., 2000; Kohn, 2017). The absence of a strong negative Nb-Ta anomaly in pargasite from the oxide gabbronoritic band (Fig. 12f) agrees with the minor Fe-Ti oxide phases precipitation along the contact.

The textural phase relationships therefore point to formation of the oxide gabbronoritic band by crystallization of an infiltrating melt. The extremely chemically evolved compositions of the mineral phases overlap with those of undeformed oxide gabbros, sharing similar Mg#, Al_2O_3, Ti and Y-REE contents in pargasite (Figs. 9, 12), Mg# in clinopyroxene (Supplementary Figure S1) and An component in plagioclase (Fig. 10a). Hence, the infiltrated melt was an late-stage differentiated MORB likely migrating from an olivine gabbro that crystallized deeper in the crustal sequence. It is worth noting the presence of euhedral orthopyroxene in the oxide gabbronoritic band. This finding contrasts with the typical occurrence of orthopyroxene as late-stage interstitial and vermicular crystals (e.g., Natland et al., 1991; Ozawa et al., 1991; Feig et al., 2006; Botcharnikov et al., 2008; Koepke et al., 2018) and with a MORB magmatic crystallization process predicted by laboratory experiments (e.g., Grove et al., 1992). Instead, it indicates early orthopyroxene saturation in the gabbronorite-forming melt. Gardner et al. (2020) and Zhang et al. (2020) also documented the occurrence of substantial amounts of neoblastic orthopyroxene (up to 20 vol%) in deformed olivine gabbros from the Atlantis Bank OCC lower crustal section. They interpreted the unexpected modal compositions as resulting from reactions between an oxide-saturated melt and a primitive gabbroic crystal mush. This reactive process was successfully reproduced by thermodynamic modelling of reactive fractional crystallization by Basch et al. (submitted). Based on the structural and textural relationships between the host mylonite and the oxide gabbronoritic band, we propose that the band crystallized from a melt that infiltrated with the host deformed olivine gabbro.

Contrasting degrees of deformation are observed between the oxide gabbronoritic band and the host mylonite. Larger grains in the former show undulose extinction and suggest that the band underwent deformation at high temperature conditions mainly accommodated by dislocation creep, but also indicate that no further strain was localized in that zone. In contrast, the remarkable grain-size reduction governed by dynamic recrystallization in the mylonitic olivine gabbro indicate that the host rock record greater extents of deformation in comparison to the oxide gabbronoritic band (e.g., Miranda & John, 2010; Gardner et al., 2020). Specifically, their crosscutting relationship implies that the host mylonitic gabbro underwent deformation prior to infiltration of the differentiated melt. The grain size reduction in the host mylonite led to an increase in grain boundaries and pore volume that facilitated melt infiltration along grain boundaries, thereby creating pathways for open system porous melt flow (e.g., Daczko et al., 2016; Meek et al., 2019; Stuart et al., 2018a; Stuart et al., 2018b; Gardner et al., 2020). At increasing melt mass, these pathways generated local channelized melt flow (e.g., Lee et al., 2018; Meek et al., 2019) that ultimately crystallized to form the oxide gabbronoritic band.

SUMMARY AND CONCLUSIONS

Although present in extremely variable modal abundances, brown amphibole is a common mineral phase in undeformed and plastically deformed gabbroic rocks from the lower oceanic crustal section at the Atlantis Bank OCC. The well-defined grain boundaries of the studied brown amphiboles, together with their low Cl contents and LREE/HREE ratios, overall high Ti contents and MORB-like $\delta^{18}O$ values, indicate that they crystallized from a hydrous melt with no involvement of seawater components. Brown amphibole thus represents a key mineral phase recording the various magmatic stages of lower crustal evolution and tracing the involvement of melt during deformation events driven by crustal exhumation.

In the undeformed gabbroic rocks, the major and trace element compositions of pargasites and then edenites, which evolve chemically from olivine gabbros to oxide gabbros and diorites, reflect the various extents of MORB magmatic differentiation experienced by the parental melts. In the most primitive olivine gabbros, the hydrous conditions necessary for amphibole saturation were achieved after >90% melt fractionation and crystallization of most anhydrous phases (i.e., olivine, plagioclase and clinopyroxene). There, the SiO_2-rich and H_2O-rich melts remained trapped interstitially between the primary minerals, leading to precipitation of interstitial pargasite. The latter occurred at decreasing temperature, from ~1000°C to ~900°C, marking the closure of the system and attainment of completely solid conditions. Prior to this stage of olivine gabbro solidification, the crystal mush experienced various events of melt migration and extraction testified by clinopyroxene and plagioclase compositions, ultimately leading to the formation of the grain-size variations that characterize Hole U1473A. Clinopyroxene in fine-grained olivine gabbros and those from the studied oxide gabbros share similar absolute concentrations of incompatible trace elements and show overall comparable LREE/HREE ratios, indicating that they crystallized from melts having similar compositions. This suggests that aliquots of melts which accumulated to form the fine-grained olivine gabbros escaped, possibly driven by further compaction, and migrated through the lower oceanic crust. These late-stage differentiated MORB-type melts accumulated in discrete intervals where advanced crystallization triggered extreme melt chemical evolution, thereby promoting a rapid Si-enrichment in the residual melt. The closed-system crystallization of these late-stage differentiated MORB led to the local formation of the oxide gabbros, whereas the extremely differentiated melts extracted from such discrete intervals ultimately formed the diorite veins.

In mylonitic intervals, mineral compositions overlap with those of the undeformed olivine gabbros; the pargasites are nearly identical. Within the crystal plastic fabric, the occurrence of stretched anhedral grains of pargasite suggests that melt was still present interstitially in the olivine gabbro during the initiation of the plastic deformation event. Thus, plastic deformation initiated in a melt-bearing olivine gabbro, consistently with the high equilibrium temperatures computed from the pargasitic amphiboles chemistry. Continuous deformation and related grain-size reduction led to a progressive increase in porosity, in turn promoting infiltration of late-stage differentiated MORBs migrating through the lower oceanic crust.

ACKNOWLEDGEMENTS

The Authors would like to thank Andrea Risplendente for his assistance with EPMA analyses at Università degli Studi di Milano, as well as Antonio Langone for his assistance with the LA-ICP-MS analyses at the CNR-IGG, Unità di Pavia. We are thankful to the LG-SIMS-Nancy team for their assistance in oxygen isotopes analyses. This research was funded through MUR for ECORD-IODP Italia provided to C. Ferrando and also supported by the Italian Programma di Rilevante Interesse Nazionale through the grant [PRIN 2017 Prot.2017KX5ZX8]. This research used samples and data provided by the Integrated Ocean Drilling Program (IODP).

DATA AVAILABILITY

The data underlying this article are available in the article and in its online supplementary material.

REFERENCES

Allard, M., Ildefonse, B., Oliot, É. & Barou, F. (2021). Plastic deformation of plagioclase in oceanic gabbro accreted at a slow-spreading ridge (Hole U1473A, Atlantis Bank, Southwest Indian Ridge). *Journal of Geophysical Research: Solid Earth* 126, e2021JB021964, https://doi.org/10.1029/2021JB021964.

Alt, J. C. & Bach, W. (2006). Oxygen isotope composition of a section of lower oceanic crust, ODP Hole 735B. *Geochemistry, Geophysics, Geosystems* 7, Q12008, http://dx.doi.org/10.1029/2006GC001385.

Baines, A. G., Cheadle, M. J., Dick, H. J. B., Hosford Sheirer, A., John, B. E., Kusznir, N. & Matsumoto, T. (2007). Evolution of the Southwest Indian Ridge from 55°45′E to 62°E: changes in plate-boundary geometry since 26 Ma. *Geochemistry, Geophysics, Geosystems* 8, Q06022, https://doi.org/10.1029/2006GC001559.

Baines, A. G., Cheadle, M. J., John, B. E., & Schwartz, J. J. (2008). The rate of oceanic detachment faulting at Atlantis Bank, SW Indian Ridge. *Earth and Planetary Science Letters* 273, 105–114, https://doi.org/10.1016/j.epsl.2008.06.013.

Basch, V., Sanfilippo, A., Sani, C., Ohara, Y., Snow, J., Ishizuka, O., Harigane, Y., Michibayashi, K., Sen, A., Akizawa, N., Okino, K., Fujii, M. & Yamashita, H. (2020). Crustal accretion in a slow-spreading back-arc basin: Insights from the Mado Megamullion oceanic core complex in the Shikoku Basin. *Geochemistry, Geophysics, Geosystems* 21, e2020GC009199, https://doi.org/10.1029/2020gc009199.

Basch, V., Drury, M. R., Plumper, O., Hellebrand, E., Crispini, L., Barou, F., Godard, M., & Rampone, E. (2021). Intracrystalline melt migration in deformed olivine revealed by trace element compositions and polyphase solid inclusions. *European Journal of Mineralogy* 33, 463–477, https://doi.org/10.5194/ejm-33-463-2021.

Beccaluva, L., Chinchilla-Chaves, A. L., Coltorti, M., Giunta, G., Siena, F. & Vaccaro, C. (1999). Petrological and structural significance of the Santa Elena-Nicoya ophiolitic complex in Costa Rica and geodynamic implications. *European Journal of Mineralogy* 11, 1091–1107.

Berndt, J., Koepke, J. & Holtz, F. (2005). An experimental investigation of the influence of water and oxygen fugacity on differentiation of MORB at 200 MPa. *Journal of Petrology* 46, 135–167, https://doi.org/10.1093/petrology/egh066.

Bindeman, I. N. (2008). Oxygen isotopes in mantle and crustal magmas as revealed by single crystal analysis. *Reviews in Mineralogy and Geochemistry* 69, 445–478, https://doi.org/10.2138/rmg.2008.69.12.

Blackman, D. K., Ildefonse, B., John, B. E., Ohara, Y., Miller, D. J., MacLeod, C. J., & the Expedition 304/305 Scientists (2006). *Proceedings of the Integrated Ocean Drilling Program* 304/305. College Station, TX: Integrated Ocean Drilling Program Manage Int. https://doi.org/10.2204/iodp.sp.304305.2004.

Bloomer, S. H., Natland, J. H., Meyer, P. S., & Dick, H. J. B. (1991). Textural and mineralogical variations in gabbroic rocks from Hole 735B. In P. T., Robins, R. P., Von Herzen, A. C., Adamson, K., Becker, S. H., Bloomer, M., Cannat, H. J. B. Dick, R. F. K., Emmermann, Q., Qard, D. D., Goldberg, R., Hebert, J. Q. H., Hertogen, H., Hoskins, G. J., Iturrino, J. D. C., Kassenaar, P. D., Kempton, E., Kikawa, S. H., Kirby, P. S., Meyer, J. H., Natland, K., Ozawa, H., Janet, J. H., Pariso, J. H., Scott, D. S., Stakes, & A., Stephen (Eds.), Proceedings of the Ocean Drilling Program, (pp. 21– 40). College Station, TX: Ocean Drilling Program.

Botcharnikov, R. E., Almeev, R., Koepke, J., Holtz, F. (2008). Phase relations and liquid lines of descent in hydrous ferrobasalt - Implications for the Skaergaard Intrusion and Columbia

River Flood Basalts. *Journal of Petrology* 49, 1687-1727, https://doi.org/10.1093/petrology/egn043.

Boulanger, M., France, L., Deans, J. R., Ferrando, C., Lissenberg, J., & von der Handt, A. (2020). Magma reservoir formation and evolution at a slow-spreading center (Atlantis Bank, Southwest Indian Ridge). *Frontiers in Earth Sciences* 8, 554598, https://doi.org/10.3389/feart.2020.554598.

Boulanger, M., France, L., Ferrando, C., Ildefonse, B., Ghosh, B., Sanfilippo, A., et al. (2021). Magma-mush interactions in the lower oceanic crust: Insights from Atlantis Bank layered series (Southwest Indian Ridge). *Journal of Geophysical Research: Solid Earth* 126, e2021JB022331, https://doi.org/10.1029/2021JB022331.

Bucholz, C. E., Jagoutz, O., VanTongeren, J. A., Setera, J. & Wang, Z. (2017). Oxygen isotope trajectories of crystallizing melts: Insights from modeling and the plutonic record. *Geochimica et Cosmochimica Acta* 207, 154–184, https://dx.doi.org/10.1016/j.gca.2017.03.027.

Cannat, M. (1991). Plastic deformation at an oceanic spreading ridge: a microstructural study of the site 735 gabbros (Southwest Indian Ocean). *Proceedings of the Ocean Drilling Program: Scientific Results* 118, 399–408, https://doi.org/10.2973/odp.proc.sr.118.134.1991.

Cannat, M., Mevel, C. & Stakes, D. (1991). Normal ductile shear zones at an oceanic spreading ridge: tectonic evolution of site 735 gabbros (Southwest Indian Ocean). In: Von Herzene, RP a RPT (ed) *Proceedings of the Ocean Drilling Program, Scientific Results*. Ocean Drilling Program, College Station, pp 415–430, https://doi.org/10.2973/odp.proc.sr.118.157.1991.

Casini, L., Maino, M., Sanfilippo, A., Ildefonse, B. & Dick, H.J.B. (2021). High-Temperature Strain Localization and the Nucleation of Oceanic Core Complexes (16.5°N, Mid-Atlantic Ridge). *Journal of Geophysical Research: Solid Earth* 126(9), pp.e2021JB022215, https://doi.org/10.1029/2021jb022215.

Chen, Y., Niu, Y., Wang, X., Gong, H., Guo, P., Gao, Y., & Shen, F. (2019). Petrogenesis of ODP hole 735B (Leg 176) oceanic plagiogranite: Partial melting of gabbros or advanced extent of fractional crystallization? *Geochemistry, Geophysics, Geosystems* 20, 2717–2732, https://doi.org/10.1029/2019GC008320.

Coleman, R. G. & Donato, M. M. (1979). Oceanic plagiogranite revisited. In: Barker, F. (ed.) Trondhjemites, dacites, and related rocks. Elsevier, Amsterdam, pp 149–167, https://doi.org/10.1016/B978-0-444-41765-7.50010-1.

Coogan, L. A & O'Hara, M. J. (2015). MORB differentiation: In situ crystallization in replenished-tapped magma chambers. *Geochimica et Cosmochimica Acta* 158, 147-161, https://doi.org/10.1016/j.gca.2015.03.010.

Coogan, L. A., Saunders, A. D., Kempton, P. D. & Norry, M. J. (2000). Evidence from oceanic gabbros for porous melt migration within a crystal mush beneath the Mid-Atlantic Ridge. *Geochemistry, Geophysics, Geosystems* 1(9), https://doi.org/10.1029/2000GC000072.

Coogan, L. A., Wilson, R. N., Gillis, K. M. & MacLeod, C. J. (2001). Near-solidus evolution of oceanic gabbros: Insights from amphibole geochemistry. *Geochimica et Cosmochimica Acta* 65, 4339–4357, https://doi.org/10.1029/2000GC000072.

Coogan, L. A., Thompson, G. M., MacLeod, C. J., Dick, H. J. B., Edwards, S., Hosford Scheirer, A. & Barry, T. (2004). A combined basalt and peridotite perspective on 14 million years of melt generation at the Atlantis Bank segment of the Southwest Indian Ridge: Evidence for temporal changes in mantle dynamics? *Chemical Geology* 207, 13–30, https://doi.org/10.1016/j.chemgeo.2004.01.016.

Cortesogno, L., Gaggero, L. & Zanetti, A. (2000). Rare earth and trace elements in igneous and high-temperature metamorphic minerals of oceanic gabbros (MARK area, Mid-Atlantic Ridge). *Contributions to Mineralogy and Petrology* 139, 373–393, https://doi.org/10.1007/s004100000147.

Daczko, N. R., Piazolo, S., Meek, U., Stuart, C. A. & Elliott, V. (2016). Hornblendite delineates zones of mass transfer through the lower crust. *Scientific Reports* 6, 31369, https://doi.org/10.1038/srep31369.

Das, P., Iyer, S. D. & Hazra, S. (2012). Petrological characteristics and genesis of the Central Indian Ocean Basin basalts. *Acta Geologica Sinica* 86, 1154–1170, https://doi.org/10.1111/j.1755-6724.2012.00738.x.

DePaolo, D. J. (1981). Trace element and isotopic effects of combined wall-rock assimilation and fractional crystallization. *Earth and Planetary Science Letters* 53, 189–202, https://doi.org/10.1016/0012-821X(81)90153-9.

Dick, H. J. B., MacLeod, C. J., Blum, P., Abe, N., Blackman, D. K., Bowles, J. A., et al. (2019). Dynamic accretion beneath a slow-spreading ridge segment: IODP Hole 1473A and the Atlantis Bank Oceanic Core Complex. *Journal of Geophysical Research: Solid Earth* 124, 12631–12659, https://doi.org/10.1029/2018JB016858.

Dick, H. J. B., Natland, J. H., Alt, J. C., Bach, W., Bideau, D., Gee, J. S., et al. (2000). A long in situ section of the lower ocean crust: Results of ODP Leg 176 drilling at the Southwest Indian Ridge. *Earth and Planetary Science Letters* 179, 31–51, https://doi.org/10.1016/S0012-821X(00)00102-3.

Dick, H. J. B., Ozawa, K., Meyer, P. S., Niu, Y., Robinson, P. T., Constantin, M., et al. (2002). Primary silicate mineral chemistry of a 1.5-km section of very slow spreading lower ocean crust: ODP Hole 753B, Southwest Indian Ridge. *Proceedings of the Ocean Drilling Program* 176, 1–61, https://doi.org/10.2973/odp.proc.sr.176.001.2002.

Dick, H. J. B., Schouten, H., Meyer, P. S., Gallo, D. G., Bergh, H., Tyce, R., et al. (1991). Tectonic evolution of the Atlantis II Fracture Zone. In: R. P., Von Herzen, & P. T., Robinson (Eds.), *Proceedings of the Ocean Drilling Program, Scientific Results* 118, 359–398. College Station, TX: Ocean Drilling Program, https://doi.org/10.2973/odp.proc.sr.118.156.1991.

Dick, H. J. B., Kvassnes, A. J. S., Robinson, P. T., MacLeod, C. J. & Kinoshita, H. (2019a). The Atlantis Bank Gabbro Massif, Southwest Indian Ridge. Progress in Earth and Planetary Science 6, 64, https://doi.org/10.1186/s40645-019-0307-9.

Dick, H. J. B., Macleod, C. J., Blum, P., Abe, N., Blackman, D. K., Bowles, J. A., Cheadle, M. J., Cho, K., Ciazela, J., Deans, J. R., Edgcomb, V. P., Ferrando, C., France, L., Ghosh, B., Ildefonse, B., John, B., Kendrick, M. A., Koepke, J., Leong, J. A. M., Liu, C., Ma, Q., Morishita, T., Morris, A., Natland, J.H., Nozaka, T., Pluemper, O., Sanfilippo, A., Sylvan, J. B., Tivey, M. A., Tribuzio, R. & Viegas, G. (2019b). Dynamic accretion beneath a slow-spreading ridge segment: IODP Hole 1473A and the Atlantis Bank Oceanic Core complex. *Journal of Geophysical Research: Solid Earth* 124, 2631–12659, https://doi.org/10.1029/2018JB016858.

Eiler, J. M. (2001). Oxygen isotope variations of basaltic lavas and upper mantle rocks. *Reviews in Mineralogy and Geochemistry* 43, 319–364, https://doi.org/10.2138/gsrmg.43.1.319.

Ernst, W. G., & Liu, J. (1998). Experimental phase-equilibrium study of Al- and Ti-contents of calcic amphibole in MORB— A semiquantitative thermobarometer. *American Mineralogist,* 83(9–10), 952–969, https://doi.org/10.2138/am-1998-9-1004.

Etheridge, M. A. & Wilkie, J. C. (1979). Grain size reduction, grain boundary sliding and the flow strength of mylonites. *Tectonophysics* 58, 159–178, https://doi.org/10.1016/0040-1951(79)90327-5.

Feig, S., Koepke, J. & Snow, J. (2006). Effect of water on tholeiitic basalt phase equilibria: an experimental study under oxidizing conditions. *Contributions to Mineralogy and Petrology* 152, 611–638, https://doi.org/10.1007/s00410-006-0123-2.

Feig, S., Koepke, J. & Snow, J.E. (2010). Effect of oxygen fugacity and water on phase equilibria of a hydrous tholeiitic basalt. *Contributions to Mineralogy and Petrology* 159, https://doi.org/10.1007/s00410-00010-00493-00413.

Ferrando, C., France, L., Basch, V., Sanfilippo, A., Tribuzio, R. & Boulanger, M. (2021a). Grain size variations record segregation of residual melts in slow-spreading oceanic crust (Atlantis Bank, 57°E Southwest Indian Ridge). *Journal of Geophysical Research: Solid Earth* 126, e2020JB020997, https://doi.org/10.1029/2020JB020997.

Ferrando, C., Basch, V., Ildefonse, B., Deans, J., Sanfilippo, A., Barou, F. & France, L. (2021b). Role of compaction in melt extraction and accumulation at a slow spreading center: Microstructures of olivine gabbros from the Atlantis Bank (IODP Hole U1473A, SWIR). *Tectonophysics* 815, 229001, https://doi.org/10.1016/j.tecto.2021.229001.

France, L., Demacon, M., Gurenko, A. A. & Briot, D. (2016). Oxygen isotopes reveal crustal contamination and a large, still partially molten magma chamber in Chaîne des Puys (French Massif Central). *Lithos* 260, 328-338, https://doi.org/10.1016/j.lithos.2016.05.013.

France, L., Ildefonse, B., & Koepke, J. (2013). Hydrous magmatism triggered by assimilation of hydrothermally altered rocks in fossil oceanic crust (Northern Oman ophiolite). *Geochemistry, Geophysics, Geosystems* 14, 2598–2614, https://doi.org/10.1002/ggge.20137.

France, L., Koepke, J., Ildefonse, B., Cichy, S. B., & Deschamps, F. (2010). Hydrous partial melting in the sheeted dike complex at fast spreading ridges: Experimental and natural observations. *Contributions to Mineralogy and Petrology* 160(5), 683–704, https://doi.org/10.1007/s00410-010-0502-6.

France, L., Lombard, M., Nicollet, C., Berthod, C., Debret, B., Koepke, J., et al. (2021). Quantifying the axial magma lens dynamics at the roof of oceanic magma reservoirs (dike/gabbro transition): Oman drilling project GT3 site survey. *Journal of Geophysical Research: Solid Earth* 126, e2020JB021496, https://doi.org/10.1029/2020JB021496.

Frost, B. R., Chamberlain, K. R., & Schumacher, J. C. (2000). Sphene (titanite): Phase relations and role as a geochronometer. *Chemical Geology* 172, 131–148, https://doi.org/10.1016/S0009-2541(00)00240-0.

Gaggero, L. & Cortesogno, L. (1997). Metamorphic evolution of oceanic gabbros: recrystallization from subsolidus to hydrothermal conditions in the MARK area (ODP Leg 153). *Lithos* 40, 105-131, 10.1016/S0024-4937(97)00006-6.

Gale, A., Dalton, C. A., Langmuir, C. H., Su, Y., Schilling, J. G. (2013). The mean composition of ocean ridge basalts. *Geochemistry, Geophysics, Geosystems* 14, 489–518, https://doi.org/10.1029/2012GC004334.

Gao, Y., Hoefs, J., Przybilla, R. & Snow, J. E. (2006). A complete oxygen isotope profile through the lower oceanic crust, ODP Hole 735B. *Chemical Geology* 233, 217–234, https://doi.org/10.1016/j.chemgeo.2006.03.005.

Gao, Y., Hoefs, J., Hellebrand, E., von der Handt, A. & Snow, J. (2007). Trace element zoning in pyroxenes from ODP Hole 735B gabbros: Diffusive exchange or synkinematic crystal fractionation? *Contributions to Mineralogy and Petrology* 153, 429–442, https://doi.org/10.1007/s00410-006-0158-4.

Gardner, R. L., Piazolo, S., Daczko, N. R. & Trimby, P. (2020). Microstructures reveal multistage melt present strain localisation in mid-ocean gabbros. *Lithos* 366-367, 105572, https://doi.org/10.1016/j.lithos.2020.105572.

Gillis, K. M. & Meyer, P. S. (2001). Metasomatism of oceanic gabbros by late-stage melts and hydrothermal fluids: Evidence from the rare earth element composition of amphiboles. *Geochemistry, Geophysics, Geosystems* 2, https://doi.org/10.1029/2000GC000087.

Ghiorso, M. S. & Sack, O. (1995). Chemical mass transfer in magmatic processes. IV. A revised and internally consistent thermodynamic model for the interpolation and extrapolation of liquid-solid equilibria in magmatic systems at elevated temperatures and pressures. *Contributions to Mineralogy and Petrology* 119, 197–212, https://doi.org/10.1007/BF00307281.

Gregory, R. T. & Taylor Jr., H. P. (1981). An oxygen-isotope profile in a section of Cretaceous oceanic crust, Samail ophiolite, Oman: evidence for $\delta^{18}O$ buffering of the oceans by deep (>5 km) seawater-hydrothermal circulation at mid-ocean ridges. *Journal of Geophysical Research* 86, 2737–2755, https://doi.org/10.1029/JB086IB04P02737.

Grove, T. L., Kinzler, R. J. & Bryan, W. B. (1992). Fractionation of Mid-Ocean Ridge Basalt (MORB). In: Phipps Morgan, J., Blackman, D. K. & Sinton, J. M. (Eds.) Mantle Flow and melt generation at mid-ocean ridges. *Geophysical Monograph Series* 71, 281-310, https://doi.org/10.1029/GM071p0281.

Harigane, Y., Okamoto, A., Morishita, T., Snow, J. E., Tamura, A., Yamashita, H., Michibayashi, K., Ohara, Y. & Arai, S. (2019). Melt–fluid infiltration along detachment shear zones in oceanic core complexes: Insights from amphiboles in gabbro mylonites from the Godzilla Megamullion, Parece Vela Basin, the Philippine Sea. *Lithos* 344–345, 217–231, https://doi.org/10.1016/j.lithos.2019.06.019.

Hauri, E. H., Gaetani, G. A., Green, T. H. (2006). Partitioning of water during melting of the Earth's upper mantle at H2O-undersaturated conditions. *Earth and Planetary Science Letters* 248, 715-734, https://doi.org/10.1016/j.epsl.2006.06.014.

Holland, T. & Blundy, J. (1994). Non-ideal interactions in calcic amphiboles and their bearing on amphibole–plagioclase thermometry. *Contributions to Mineralogy and Petrology* 116, 433–447, https://doi.org/10.1007/BF00310910.

Husen, A., Almeev, R. & Holtz, F. (2016). The effect of H_2O and Pressure on multiple saturation and liquid lines of descent in basalt from the Shatsky Rise. *Journal of Petrology* 57, 309–344, https://doi.org/10.1093/petrology/egw008.

Irving, A. J. (1978). A review of experimental studies of crystal/liquid trace element partitioning. *Geochimica Cosmochimica Acta* 42, 743-770, https://doi.org/10.1016/0016-7037(78)90091-1.

Jaroslow, G. E., Hirth, G. & Dick, H. J. B. (1996). Abyssal peridotite mylonites: implications for grain-size sensitive flow and strain localization in the oceanic lithosphere. *Tectonophysics* 256, 17-37, https://doi.org/10.1016/0040-1951(95)00163-8.

John, B. E., Foster, D. A., Murphy, J. M., Cheadle, M. J., Baines, A. G., Fanning, C. M., & Copeland, P. (2004). Determining the cooling history of in situ lower oceanic crust-Atlantis Bank, SW Indian Ridge. *Earth and Planetary Science Letters* 222, 145–160, https://doi.org/10.1016/j.epsl.2004.02.014.

Johnson, M. C., Anderson, A. T. & Rutherford, M. J. (1994). Pre-eruptive volatile contents of magmas. In: Carroll, M.R., Holloway, J.R. (Eds.), Volatiles in magmas. *Mineralogical Society of America, Washington, DC, United States*, pp. 281–330.

Klemme, S., Günther, D., Hametner, K., Prowatke, S., Zack, T. (2006). The partitioning of trace elements between ilmenite, ulvospinel, armalcolite and silicate melts with implications for the early differentiation of the moon. *Chemical Geology* 234, 251-263, https://doi.org/10.1016/j.chemgeo.2006.05.005.

Klinkhammer, G. P., Elderfield, H., Edmond, J. M. & Mitra, A. (1994). Geochemical implications of rare earth element patterns in hydrothermal fluids from mid-ocean ridges. *Geochimica et Cosmochimica Acta* 58, 5105-5113, http://doi.org/10.1016/0016-7037(94)90297-6.

Koepke, J., Berndt, J., Feig, S. T. & Holtz, F. (2007). The formation of SiO_2-rich melts within the deep oceanic crust by hydrous partial melting of gabbros. *Contributions to Mineralogy and Petrology* 153, 67–84, https:// doi.org/10.1007/s00410-006-0135-y.

Koepke, J., Botcharnikov, R. E. & Natland, J. H. (2018). Crystallization of late-stage MORB under varying water activities and redox conditions: Implications for the formation of highly evolved lavas and oxide gabbro in the ocean crust. *Lithos* 323, 58–77, https://doi.org/10.1016/j.lithos.2018.10.001.

Koepke, J., Feig, S. T., Snow, J. & Freise, M. (2004). Petrogenesis of oceanic plagiogranites by partial melting of gabbros: An experimental study. *Contributions to Mineralogy and Petrology* 146, 414–432, https://doi.org/10.1007/s00410-003-0511-9.

Koepke, J., Berndt, J., & Busy, F. (2003). An experimental study on the shallow-level migmatization of ferrogabbros from the Fuerteventura Basal Complex, Canary islands. *Lithos* 69, 105–125, https://doi.org/10.1016/S0024-4937(03)00049-5.

Koepke, J., France, L., Müller, T., Faure, F., Goetze, N., Dziony, W. & Ildefonse, B. (2011). Gabbros from IODP Site 1256, equatorial Pacific: Insight into axial magma chamber processes at fast spreading ocean ridges. *Geochemistry, Geophysics, Geosystems* 12, Q09014, https://doi.org/10.1029/2011GC003655.

Kohn, M. (2017). Titanite Petrochronology. *Reviews in Mineralogy & Geochemistry* 83, 419-441, https://doi.org/10.2138/rmg.2017.83.13.

Lackey, J. S., Valley, J. W., Chen, J. H. & Stockli, D. F. (2008). Dynamic magma systems, crustal recycling, and alteration in the central Sierra Nevada Batholith: the oxygen isotope record. *Journal of Petrology* 49, 1397–1426, https://doi.org/10.1093/petrology/egn030.

Leake, B. E., Woolley, A. R., Arps, C. E. S., et al. (1997). Nomenclature of amphiboles: Report of the subcommittee on amphiboles of the International Mineralogical Association Commission on new minerals and mineral names. *American Mineralogist* 82, 1019–1037.

Lee, A. L., Torvela, T., Lloyd, G. E. & Walker, A.M. (2018). Melt organisation and strain partitioning in the lower crust. *Journal of Structural Geology* 113, 188–199, https://doi.org/10.1016/j.jsg.2018.05.016.

le Roex, A. P., Dick, H. J. B., Reid, A. M., Erlank, A. J. (1982). Ferrobasalts from the Spiess ridge segment of the Southwest Indian ridge. *Earth and Planetary Science Letters* 60, 437-451, https://doi.org/10.1016/0012-821X(82)90079-6.

Lissenberg, C. J., & MacLeod, C. J. (2016). A reactive porous flow control on mid-ocean ridge magmatic evolution. *Journal of Petrology* 57, 2195–2220, http://doi.org/10.1093/petrology/egw074.

Loocke, M. P. (2016). The role of the axial melt lens in crustal accretion at fast spreading mid-ocean ridges. PhD thesis. Cardiff (Wales): Cardiff University, pp.191.

Ma, Q., Dick, H. J. B., Urann, B. & Zhou, H. (2020). Silica-rich vein formation in an evolving stress field, Atlantis Bank Oceanic core complex. *Geochemistry, Geophysics, Geosystems* 21, e2019GC008795, https://doi.org/10.1029/2019GC008795.

MacLeod, C. J., Dick, H. J. B., Blum, P. & the Expedition 360 Scientists (2017). Southwest Indian Ridge Lower Crust and Moho. *Proceedings of the International Ocean Discovery Program* 360. College Station, TX: International Ocean Discovery Program, pp. 1–51.

Meek, U., Piazolo, S. & Daczko, N. R. (2019). The field and microstructural signatures of deformation-assisted melt transfer: insights from magmatic arc lower crust, New Zealand. *Journal of Metamorphic Geology* 37, 795–821.

Mehl, L. & Hirth, G. (2008). Plagioclase preferred orientation in layered mylonites: evaluation of flow laws for the lower crust. *Journal of Geophysical Research: Solid Earth* 113, B05202, https://doi.org/10.1029/2007JB005075.

Merzbacher, C. & Eggler, D.H. (1984). A magmatic geohygrometer: application to Mount St. Helens and other dacitic magmas. *Geology* 12, 587–590.

Miranda, E. A. & John, B. E. (2010). Strain localization along the Atlantis Bank oceanic detachment fault system, Southwest Indian Ridge. *Geochemistry, Geophysics, Geosystems* 11, Q04002, https://doi.org/10.1029/2009GC002646.

Muehlenbachs, K. & Byerly, G. R. (1982). ^{18}O-enrichment of silicic magmas caused by crystal fractionation at the Galapagos Spreading Center. *Contributions to Mineralogy and Petrology* 79, 76–79.

Nandedkar, R. H., Hurlimann, N., Ulmer, P. & Muntener, O. (2016). Amphibole–melt trace element partitioning of fractionating calc-alkaline magmas in the lower crust: An experimental study. *Contributions to Mineralogy and Petrology* 171, 71, https://doi.org/10.1007/s00410-016-1278-0.

Natland, J. H., & Dick, H. J. B. (2001). Formation of the lower ocean crust and the crystallization of gabbroic cumulates at a very slow spreading ridge. *Journal of Volcanology and Geothermal Research* 110, 191–233, https://doi.org/10.1016/S0377-0273(01)00211-6.

Natland, J. H., Meyer, P. S., Dick, H. J. B. & Bloomer, S. H. (1991). Magmatic oxides and sulfides in gabbroic rocks from ODP Hole 735B and the later development of the liquid line of descent. In: Von Herzen, R.P., Robinson, P.T., et al. (Eds.), *Proceedings of the Ocean Drilling Program, Scientific Results*. Ocean Drilling Program, College Station, TX, pp. 41–73.

Nguyen, D., Morishita, T., Soda, Y., Tamura, A., Ghosh, B., Harigane, Y., France, L., Liu, C., Natland, J. H., Sanfilippo, A., MacLeod, C., Blum, P. & Dick, H. J. B. (2018). Occurrence of felsic rocks in oceanic gabbros from IODP hole 1473A: Implications for evolved melt migration in the lower oceanic crust. *Minerals* 8, 583, https://doi.org/10.3390/min8120583.

Nicollet, C., Paquette, J.-L, Bruand, E., Bosse, V. & Pereira, I. (2022). Crystallisation and fast cooling of the (meta)gabbro from the Chenaillet ophiolite (Western Alps): In-situ U-Pb dating of zircon, titanite, monazite and xenotime in textural context. *Lithos* 414–415, 106620, https://doi.org/10.1016/j.lithos.2022.106620.

Niu, Y., Gilmore, T., Mackie, S., Greig, A. & Bach, W. (2002). Mineral chemistry, whole-rock compositions, and petrogenesis of Leg 176 gabbros: Data and discussion. In: Natland, J. H., Dick, H. J. B., Miller, D. J. & Von Herzen, R. P. (eds) *Proceedings of the Ocean Drilling Program, Scientific Results* 176. College Station, TX: Ocean Drilling Program, 1–60.

Ozawa, K., Meyer, P. S. & Bloomer, S. H. (1991). Mineralogy and textures of iron-titanium-oxide gabbros from hole 735B. In: Von Herzen, R.P., Robinson, P.T., et al. (Eds.), *Proceedings of the Ocean Drilling Program, Scientific Results*. Ocean Drilling Program, College Station, TX, 118, 41–73, doi: 10.2973/odp.proc.sr.118.125.1991.

Palmiotto, C., Corda, L., Ligi, M., Cipriani, A., Dick, H. J. B., Douville, E., Gasperini, L., Montagna, P., Thil, F., Borsetti, A. M., Balestra, B., & Bonatti, E. (2013). Nonvolcanic tectonic islands in ancient and modern oceans. *Geochemistry, Geophysics, Geosystems* 14, 4698–4717, https:// doi.org/10.1002/ggge.20279.

Palmiotto, C., Corda, L. & Bonatti, E. (2017). Oceanic tectonic islands. *Terra Nova* 29, 1-12, https://doi.org/10.1111/ter.12247.

Pearce, N. J. G., Perkins, W. T., Westgate, J. A., Gorton, M. P., Jackson, S. E., Neal, C. R., & Chenery, S. P. (1997). A compilation of new and published major and trace element data for NIST SRM 610 and NIST SRM 612 glass reference materials. *Geostandards Newsletter: The Journal of Geostandards and Geoanalysis* 21, 115–144, https://doi.org/10.1111/j.1751-908X.1997.tb00538.x.

Pettigrew, T. L., Casey, J. F., Miller, D. J., et al. (1999). Proceedings of the Ocean Drilling Program, Initial Reports, 179: College Station, TX (Ocean Drilling Program). http://dx.doi.org/10.2973/odp.proc.ir.179.1999.

Pieterek, B., Ciazela, J., Boulanger, M., Lazarov, M., Wegorzewski, A. V., Pańczyk, M., Strauss, H., Dick, H. J. B., Muszyński, A., Koepke, J., Kuhn, T., Czupyt, Z., France, L. (2022). Sulfide enrichment along igneous layer boundaries in the lower oceanic crust: IODP Hole U1473A, Atlantis Bank, Southwest Indian Ridge. *Geochimica et Cosmochimica Acta* 320, 179-206, https://doi.org/10.1016/j.gca.2022.01.004.

Putirka, K. (2016). Amphibole thermometers and barometers for igneous systems and some implications for eruption mechanisms of felsic magmas at arc volcanoes. *American Mineralogist* 101, 841–858, https://doi.org/10.2138/am-2016-5506.

Righter, K., Leeman, W. P. & Hervig, R. L. (2006). Partitioning of Ni, Co and V between spinel-structured oxides and silicate melts: Importance of spinel composition. *Chemical Geology* 227, 1-25, https://doi.org/10.1016/j.chemgeo.2005.05.011.

Rioux, M., Cheadle, M. J., John, B. E. & Bowring, S. A. (2016). The temporal and spatial distribution of magmatism during lower crustal accretion at an ultraslow-spreading ridge: High-precision U–Pb zircon dating of ODP Holes 735B and 1105A, Atlantis Bank, Southwest Indian Ridge. *Earth and Planetary Science Letters* 449, 395–406, https://doi.org/10.1016/j.epsl.2016.05.047.

Robinson, P.T., Von Herzen, R.P. et al. (1991). Proceedings of the Ocean Drilling Program. Initial Reports, College Station, Texas, p. 826.

Sanfilippo, A., Dick, H. J. B., Marschall, H. R., Lissenberg, C. J. & Urann B. (2019). Emplacement and high-temperature evolution of gabbros of the 16.5°N oceanic core complexes (Mid-Atlantic Ridge): Insights into the compositional variability of the lower oceanic crust. *Geochemistry, Geophysics, Geosystems* 20, 46-66, https://doi.org/10.1029/2018GC007512.

Sanfilippo, A., MacLeod, C. J., Tribuzio, R., Lissenberg, C. J. & Zanetti, A. (2020). Early-stage melt-rock reaction in a cooling crystal mush beneath a slow-spreading mid-ocean ridge (IODP Hole U1473A, Atlantis Bank, Southwest Indian Ridge). *Frontiers in Earth Science* 8, 579138, https://doi.org/10.3389/feart.2020.579138.

Schwartz, J. J., John, B. E., Cheadle, M. J., Miranda, E. A., Grimes, C. B., Wooden, J. L. & Dick, H. J. B. (2005). Dating the growth of oceanic crust at a slow-spreading ridge. *Science* 310, 654–657, https://doi.org/10.1126/science.1116349.

Shimizu, K., Liang, Y., Sun, C., Jackson, C. R. & Saal, A. E. (2017). Parameterized lattice strain models for REE partitioning between amphibole and silicate melt. *American Mineralogist* 102, 2254–2267, https://doi.org/10.2138/am-2017-6110.

Sobolev, A. V., Chaussidon, M. (1996). H_2O concentrations in primary melts from supra-subduction zones and mid-ocean ridges: Implications for H_2O storage and recycling in the mantle. *Earth and Planetary Science Letters* 137, 45-55, https://doi.org/10.1016/0012-821X(95)00203-O.

Stakes, D., Mével, C., Cannat, M. & Chaput, T. (1991). Metamorphic stratigraphy of Hole 735B, *Proceedings of the Ocean Drilling Program Scientific Results* 118, 153–181.

Stuart, C. A., Meek, U., Daczko, N. R., Piazolo, S. & Huang, J. X. (2018a). Chemical Signatures of Melt–Rock Interaction in the Root of a Magmatic Arc. *Journal of Petrology* 59, 321–340, https://doi.org/10.1093/petrology/egy029.

Stuart, C. A., Piazolo, S. & Daczko, N. R. (2018b). The recognition of former melt flux through high-strain zones. *Journal of Metamorphic Geology* 36, 1049-1069, https://doi.org/10.1111/jmg.12427.

Sun, C. & Liang, Y. (2012). Distribution of REE between clinopyroxene and basaltic melt along a mantle adiabat: effects of major element composition, water and temperature. *Contributions to Mineralogy and Petrology* 163, 807–823. https://doi.org/10.1007/s00410-011-0700-x.

Sun, C., Graff, M., & Liang, Y. (2017). Trace element partitioning between plagioclase and silicate melt: The importance of temperature and plagioclase composition, with implications for terrestrial and lunar magmatism. *Geochimica et Cosmochimica Acta* 206, 273–295, https://doi.org/10.1016/j.gca.2017.03.003.

Tamura, A., Morishita, T., Ishimaru, S., Hara, K., Sanfilippo, A. & Arai, S. (2016). Compositional variations in spinel-hosted pargasite inclusions in the olivine-rich rock from the oceanic crust–mantle boundary zone. *Contributions to Mineralogy and Petrology* 171, 39, https://doi.org/10.1007/s00410-016-1245-9.

Taufner, R., Viegas, G., Meira Faleiros, F., Castellan, P. & Silva, R. (2021). Deformation mechanisms of granulite-facies mafic shear zones from hole U1473A, Atlantis Bank, Southwest Indian Ridge (IODP Expedition 360). *Journal of Structural Geology* 149, 104380, https://doi.org/10.1016/j.jsg.2021.104380.

Tiepolo, M. (1999). Determinazione sperimentale dei coefficienti di distribuzione solido/liquido in anfiboli di mantello: ruolo del controllo cristallochimico. PhD Thesis, Università di Pavia, 314 pp.

Tiepolo, M., Oberti, R., Zanetti, A., Vannucci, R. & Foley, S. F. (2007). Trace-element partitioning between amphibole and silicate melt. In: Hawthorne, F. C., Oberti, R., Della Ventura, G. et al. (Eds.) Amphiboles: Crystal Chemistry, Occurrence, and Health Issues.

Reviews in Mineralogy and Geochemistry 67, 417–452, https://doi.org/10.2138/rmg.2007.67.11.

Toplis, M. J. & Carroll, M. R. (1995). An experimental study of the influence of oxygen fugacity on Fe–Ti oxide stability, phase relations, and mineral–melt equilibria in ferro-basaltic systems. *Journal of Petrology* 36, 1137–1170, https://doi.org/10.1093/petrology/36.5.1137.

Tribuzio, R., Riccardi, M. P. & Ottolini, L. (1995). Trace element redistribution in high temperature deformed gabbros from East Ligurian ophiolites (Northern Apennines, Italy): Constraints on the origin of syn-deformation fluids. *Journal of Metamorphic Geology* 13, 367–377, https://doi.org/10.1111/j.1525-1314.1995.tb00226.x.

Tribuzio, R., Tiepolo, M., Vannucci, R. & Bottazzi, P. (1999). Trace element distribution within olivine-bearing gabbros from the Northern Apennine ophiolites (Italy): Evidence for post-cumulus crystallization in MOR-type gabbroic rocks. *Contributions to Mineralogy and Petrology* 134, 123–133, https://doi.org/10.1007/s004100050473.

Tribuzio, R., Tiepolo, M. & Vannucci, R. (2000). Evolution of gabbroic rocks from the Northern Apennine ophiolites (Italy): Comparison with the lower oceanic crust from modern slow-spreading ridges. In: Dilek, J., Moores, E., Elthon, D., & Nicolas, A. (Eds.) Ophiolites and Oceanic Crust: New Insights from Field Studies and Ocean Drilling Program. *Geological Society of America, Special Papers* 349, 129–138, https://doi.org/10.1130/0-8137-2349-3.129.

Tribuzio, R., Renna, M. R., Dallai, L. & Zanetti, A. (2014). The magmatic–hydrothermal transition in the lower oceanic crust: Clues from the Ligurian ophiolites, Italy. *Geochimica et Cosmochimica Acta* 130, 188–211, https://doi.org/10.1016/j.gca.2014.01.010.

Van Achterberg, E., Ryan, C. G., Jackson, S. E., & Griffin, W. (2001). Data reduction software for LA-ICP-MS. In P. Sylvester (Ed.), Laser ablation ICP-MS in the Earth Science (pp. 239–243). *Mineralogical Association of Canada*.

Villiger, S., Ulmer, P., & Müntener, O. (2007). Equilibrium and fractional crystallization experiments at 0.7 GPa: The effect of pressure on phase relations and liquid compositions of tholeiitic magmas. *Journal of Petrology* 48, 159–184, https://doi.org/10.1093/petrology/egl058

Xirouchakis, D., Lindsley, D. H., Frost, B. R. (2001). Assemblages with titanite ($CaTiOSiO_4$), Ca-Mg-Fe olivine and pyroxenes, Fe-Mg-Ti oxides, and quartz: Part II. Application. *American Mineralogist* 86, 254–264, https://doi.org/10.2138/am-2001-2-307.

Zhang, W. Q., Liu, C. Z., & Dick, H. J. B. (2020). Evidence for multi-stage melt transport in the lower ocean crust: Atlantis Bank Gabbroic Massif (IODP Hole U1473A, SW Indian Ridge). *Journal of Petrology* 61, egaa082, https://doi.org/10.1093/petrology/egaa082.

Zhang, W. Q., Dick, H. J. B., Liu, C. Z., Lin Y. Z. & Angeloni, L. M. (2021). MORB melt transport through Atlantis Bank oceanic batholith (SW Indian Ridge). *Journal of Petrology* 62, egab034, https://doi.org/10.1093/petrology/egab034.

Zhao, Z. F. & Zheng, Y. F. (2003). Calculation of oxygen isotope fractionation in magmatic rocks. *Chemical Geology* 193, 59–80, https://doi.org/10.1016/S0009-2541(02)00226-7.

FIGURE CAPTIONS

Figure 1 – Geological setting of the Atlantis Bank OCC along the Southwest Indian Ridge. (a) Location of the Atlantis Bank OCC. (b) East-west schematic profile of Atlantis Bank vertical structure and composition modified after Dick et al. (2019a) and locations of Holes 735B and U143A.

Figure 2 – Downhole characteristics of Hole U1473A. (From left to right) Downhole lithostratigraphic variations (relative abundances of rocks are averaged over 20 m) with olivine gabbro in dark blue, gabbro in light blue, disseminated oxide gabbro in yellow, oxide-bearing gabbro in orange, oxide gabbro in red, and diabase in grey; bulk-rock Mg# (Mg# = 100 × cationic (Mg/(Mg + Fe), with all Fe as Fe^{2+}) of the recovered samples (dot colors represent the lithology as reported in the first column 'Hole U143A Lithology'); downhole intensity of crystal plastic fabrics (CPF): black line represents the 10 m running average of CPF intensity and black dots locate mylonites (CPF = 4) and ultramylonites (CPF = 5); 10 m running average of alteration intensity (grey line) and amphibole veins frequency (in blue) averaged over 10 m. CPF and alteration intensities values are from MacLeod et al., 2017.

Figure 3 – Half core images of (a) coarse-grained olivine gabbro overall undeformed to slightly deformed showing a local mylonitic to ultramylonitic shear zone, (b) poikilitic undeformed olivine gabbro displaying isotropic magmatic fabric, (c) pervasive crystal-plastic deformation in an olivine gabbro. Images from onboard core scans (MacLeod et al., 2017).

Figure 4 – Representative textures of undeformed olivine gabbro (samples (a-c) 360-U1473A-89R-6W, 4-9 cm and (d-e) 360-U1473A-89R-1W, 14-20 cm) and undeformed oxide gabbro (samples (f) 360-U1473A-81R-3W, 77-82 cm and (g) 360-U1473A-83R-1W, 13-20 cm). (a) Thin section scan of olivine gabbro under parallel-polarized light; the red box indicates the microphotograph in (c). (b) Composite Fe, Ti, Ca, P, Al compositional map of the thin section in (a); colour coding as reported in the image. (c) Close-up image from (a) showing films of interstitial brown amphibole (Amp), locally associated with small ilmenite (Ilm) crystals, along the grain boundaries of igneous phases (Ol – olivine, Pl – plagioclase, Cpx – clinopyroxene). (d) Interstitial amphibole associated with larger grains of ilmenite. (e) 'Bleb-shaped' amphibole in large clinopyroxene crystal rimmed by anhedral orthopyroxene (Opx). (f) Interstitial and 'bleb-shaped' amphibole associated with ilmenite and magnetite (Mt). (g) Large anhedral amphibole grains associated with ilmenite, magnetite, orthopyroxene and large euhedral crystals of apatite (Ap).

Figure 5 – Representative textures of dioritic intervals. (a) Contact between gabbro and diorite (yellow dotted line) marked by amphibole overgrowth on clinopyroxene of the host gabbro (sample 360-U1473A-39R-4W, 3-8 cm). The red box indicates the microphotograph in (c) and the yellow arrow points the top left corner in (c). (b) Corona of amphibole associated with ilmenite and magnetite partially enclosing and replacing clinopyroxene from the host gabbro at the contact with a dioritic interval in sample 360-U1473A-89R-3W, 108-110 cm. (c) Close-up image from (a) showing poikilitic amphibole in the core of the diorite; the amphibole encloses euhedral plagioclase, ilmenite, magnetite, apatite and zircon.

Figure 6 – Representative textures of granulite-facies mylonites. (a) Thin section scan (sample 360-U1473A- 41R-6W, 23-29 cm) under parallel-polarized light; the red boxes indicate the microphotograph in (c) and (e). (b) Composite Fe, Ti, Ca, P, Al compositional map of the thin section in (a); color coding as reported in the image. Note that high Ti contents highlight the occurrence of brown amphibole. (c-d) Close-up images (c-parallel-polarized light, d-cross-polarized light) from (a) showing deformed clinopyroxene porphyroclast (Cpx P.) mantled by the clinopyroxene (Cpx N.) + amphibole neoblastic assemblage. Orthopyroxene and apatite occur in pressure shadows at the edge of the clinopyroxene porphyroclast. Plagioclase mostly occur as neoblasts (Pl N.) and only few porphyroclasts are preserved (Pl P.). (e) Close-up image from (a) showing amphibole + apatite + ilmenite thin isolated band, and the occurrence of elongated anhedral amphibole crystals in contact with a clinopyroxene porphyroclast.

Figure 7 – Representative textures of mylonitic olivine gabbro (sample 360-U1473A-69R-1W, 23-28cm) crosscut by an oxide gabbronoritic band. (a) Thin section scan of the sample under parallel-polarized light; the full-line red box delineates the zone reported in (b), whereas the dashed red boxes indicate the microphotograph in (c) and (d). Note the euhedral crystal of titanite within the oxide gabbronoritic band. (b) Composite Fe, Ti, Ca, P, Al compositional map of zone highlighted in (a); colour coding as reported in the image. Note that high Ti contents highlight the occurrence of brown amphibole, whereas combined Ti and Fe (pink colour) and P and Al (whitish colour) mark the occurrence of ilmenite and apatite, respectively. Porphyroclastic clinopyroxene from the host mylonite (Cpx P_M) and in the band (Cpx P_B) are overgrown by secondary clinopyroxene (Cpx S). (c) Close-up image showing neoblastic plagioclase (Pl N) + ilmenite + apatite and brown amphibole + orthopyroxene levels. (d) Close-up image showing clinopyroxene porphyroclast (Cpx P) mantled by anhedral secondary clinopyroxene (Cpx S; white dashed line marks the contact). At top left corner, an aggregate of neoblastic orthopyroxene + amphibole is also present.

Figure 8 – Si a.p.f.u. (atom per formula unit) versus [Na + K] a.p.f.u. in brown amphibole from olivine gabbros, oxide gabbros, diorites and granulite-facies mylonites in IODP Hole U1473A. Amphibole classification after Leake et al. (1997). Structural formulae of amphibole were determined by assuming all iron as Fe^{2+}, positive charge = 46, and 23 oxygens.

Figure 9 – Major element compositions of brown amphiboles. Amphiboles are subdivided according to lithology and textures as reported in the legend. The composition of amphiboles in felsic veins from IODP Hole U1473A (Nguyen et al., 2018) is also reported for comparison. In granulite-facies mylonites, we distinguished amphibole in the apatite-ilmenite rich band (69-1; from sample U1473A-69R-1W, 23-28cm) from amphibole in the rest of the mylonitic intervals (41-6; mainly from sample U1473A- 41R-6W, 23-29 cm).

Figure 10 – (a) An versus K_2O (wt%) contents in plagioclase from olivine gabbros, oxide gabbros, diorites and granulite-facies mylonites in IODP Hole U1473A. Plagioclase core and plagioclase rim refer to euhedral/subhedral plagioclase in gabbros and plagioclase porphyroclasts in mylonites. The composition of plagioclase in felsic veins from IODP Hole U1473A (Nguyen et al., 2018) is also reported for comparison. (b) and (c) Histograms of distribution of An contents in plagioclase (b) and Mg# in clinopyroxene (c) obtained after

statistical analysis (QACD tool) on chemical maps. Blu colours refer to olivine gabbros, whereas yellow colours refer to mylonitic olivine gabbros.

Figure 11 – Anorthite (An) map in plagioclase (a-c-e) and maps of Mg# in olivine, pyroxenes and amphibole (b-d-f). (a) and (b) sample 360-U1473A-89R-6W, 4-9 cm reported in Figure 4. (c) and (d) sample 360-U1473A- 41R-6W, 23-29 cm reported in Figure 6. (e) and (f) sample 360-U1473A-69R-1W, 23-28cm reported in Figure 7.

Figure 12 – Chondrite-normalized Rare Earth Element (REE) concentrations (a,c,e) and extended trace element spider diagrams (b,d,f) of brown amphibole and coexisting clinopyroxene in undeformed olivine gabbros (a,b), oxide gabbros and diorites (c,d) and mylonitic olivine gabbros (e,f) from Hole U1473A. Compositional fields of brown amphiboles in other olivine gabbros and felsic veins from the same hole (Nguyen et al., 2018) are also reported for comparison. Normalizing values are after Sun and McDonough (1989).

Figure 13 – (a) Average values (per sample with 2σ error bar) of in situ $\delta^{18}O$ values of brown amphiboles in undeformed olivine gabbros (light blue) and diorites (pink) and in mylonites (yellow). The $\delta^{18}O$ compositions of magmatic clinopyroxene (Cpx, black box) and olivine (Ol, dark grey box) in olivine gabbros (Gao et al., 2006) and hydrothermal hornblende in veins (Alt & Bach, 2006; dark grey arrow on the right) from the adjacent Hole 735B are reported. For comparison, we report the $\delta^{18}O$ values of amphibole in felsic dikes and amphibole-rich gabbros from the Ligurian ophiolites (Tribuzio et al., 2014; light grey field). (b) Equilibrium temperature estimates for crystallization of brown amphibole in olivine gabbros, oxide gabbros and diorites, and for ductile deformation and development of granulite-facies mylonitic intervals in IODP Hole U1473A. Amphiboles from the granulite-facies mylonites were subdivided as reported in Figure 9, and temperature estimates were determined for neoblastic grains exclusively. Amphibole-plagioclase geothermometer (Holland & Blundy, 1994 [H&B1994]) and two single-amphibole geothermometer (Ti-Fe-Si-Na in amphibole (Amp) by Putirka, 2016 [P2016] and Ti-in amphibole by Hannover group [E&L1998*]; see text for further details) were used. Equilibrium temperatures between clinopyroxene and plagioclase rims (Cpx_R and Pl_R) determined using the geothermometer from Sun et al. (2017) for olivine gabbros (blue box) and oxide gabbros (red box) are also reported for comparison. Each column corresponds to a single sample.

Figure 14 – Major and trace element covariations in coexisting brown amphibole and clinopyroxene from undeformed olivine gabbros, oxide gabbros and diorites and mylonitic olivine gabbros sampled in Hole U1473A. (a) TiO_2 (wt%) versus Al_2O_3 (wt%) contents and (b) Ce_N/Y_N versus La_N/Sm_N (where N = Chondrite normalized values) are compared with compositions of amphibole in felsic veins from the same hole (felsic veins of magmatic origin from Nguyen et al. (2018) and Ma et al. (2020) (Type I); felsic veins as products of hydrous partial melting are Type II of Ma et al.(2020)) and magmatic amphiboles and hydrothermal amphiboles from oceanic spreading centers (Coogan et al., 2001; Gillis & Meyer, 2001; Miranda & John, 2010; Sanfilippo et al., 2019; Harigane et al., 2019) and ophiolitic analogues (Tribuzio et al., 1995, 1999, 2000). The dotted line in (b) defines the compositional field of the studied clinopyroxene, which are reported in the bottom-right inset. In the inset we also plot the

compositions of clinopyroxene from fine-grained intervals of olivine gabbros sampled in the same Hole U1473A.

Figure 15 – $\delta^{18}O$ values of computed melts in equilibrium with brown amphibole from olivine gabbros (undeformed and mylonitic) and diorites in Hole U1473A (this study; symbols and colour codes as in Fig. 14) compared with melts in equilibrium with clinopyroxene (Cpx), olivine (Ol) and plagioclase (Pl) from gabbros (blue histogram; Gao et al., 2006) and with zircons from oxide gabbros (diamond symbol) and felsic veins (pink histogram) (Pietranik et al., 2017) in Hole 735B at the Atlantis Bank OCC. The field of MORB ($d^{18}O = 5.6 \pm 0.2$) is from Eiler (2001). The $\delta^{18}O$ values of calculated equilibrium melts are compared with fractional crystallization (FC) and assimilation-fractional crystallization (AFC; see DePaolo, 1981) models. The composition of the starting melt for both models is the computed melt in equilibrium with average $\delta^{18}O$ values of pargasites in the studied undeformed olivine gabbros. Two steps of F=50% were modelled following the approach in France et al. (2016); Step$_1$ reproduces melt composition after crystallization of Ol+Pl+Cpx and Step$_2$ after crystallization of Pl+Cpx+Ox+Amp (mineral modes are reported in the legend) with predicted SiO_2 contents of 54 and 66wt%, respectively, which are comparable with hypothetic compositions of oxide gabbros and diorites parental melts. The assimilated material is set as oceanic crust altered at high temperature conditions and thus with low $\delta^{18}O$ signatures (~3‰; Stakes, 1991; Alt & Bach, 2006); the ratio crystallized/assimilated masses is 2. Used fractionation factors ($\Delta_{mineral\text{-}melt}$) are reported in the legend; because they are dependent on temperature, the $\Delta_{mineral\text{-}melt}$ were derived at suitable conditions for each lithological group (from Muehlenbachs & Byerly, 1982; Zhao & Zheng, 2003; Bindeman, 2008; France et al., 2016). $\Delta_{zircon\text{-}melt}$ is derived from Lackey et al. (2008) with $\Delta_{zircon\text{-}melt} = 0.75$ ‰ for oxide gabbros, and $\Delta_{zircon\text{-}melt} = 1.5$ ‰ for diorites and felsic veins.

Figure 16 – Computed melts in equilibrium with amphiboles and clinopyroxene from all undeformed lithologies. (a) TiO_2 (wt%) contents versus FeO/MgO ratios are compared with the database of MORBs from Gale et al. (2013) and the magmatic crystallization experiments of a ferrobasaltic melt (Koepke et al., 2018), for which we report temperature and mineral assemblage at each crystallization step (Mt = magnetite, Ilm = ilmenite, Cpx = clinopyroxene, Pl = plagioclase, Ap = apatite, Amp = amphibole). In the inset we also report the liquid line of descent of a primitive MORB, experimentally reproduced at anhydrous (dry) and hydrous (H_2O) conditions (Husen et al., 2016). Note that using partition coefficients from Nandedkar et al. (2016) (Kd_N) and Tiepolo et al. (2007) (Kd_T) to calculate melts in equilibrium with amphibole yield similar results. (b) Atlantis Bank MORB-normalized (average MORB composition from Coogan et al., 2004) REE contents in melts in equilibrium with amphiboles from the three undeformed lithologies and clinopyroxene from olivine gabbros; the melts in equilibrium with clinopyroxene from the oxide gabbros have not been calculated because of the uncertainty in the choice of the clinopyroxene/melt partition coefficients in chemically evolved systems. The dotted lines mark the minimum (Min.) and maximum (Max.) REE concentrations in ferrobasalts from the Indian Ridge (Das et al., 2012). CpxIN = analyses performed at ~50m form the clinopyroxene rim (CpxR).

Figure 17 – (a) V/Sc vs Chondrite-normalized Y and (b) Sr/Nd vs V/Y covariations in clinopyroxene and amphibole from the undeformed and deformed lithologies selected for this study.

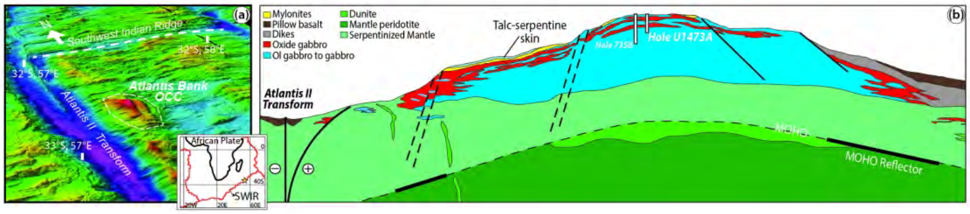

Figure 1 - Geological setting of the Atlantis Bank OCC along the Southwest Indian Ridge. (a) Location of the Atlantis Bank OCC. (b) East-west schematic profile of Atlantis Bank vertical structure and composition modified after Dick et al. (2019a) and locations of Holes 735B and U143A.

183x45mm (300 x 300 DPI)

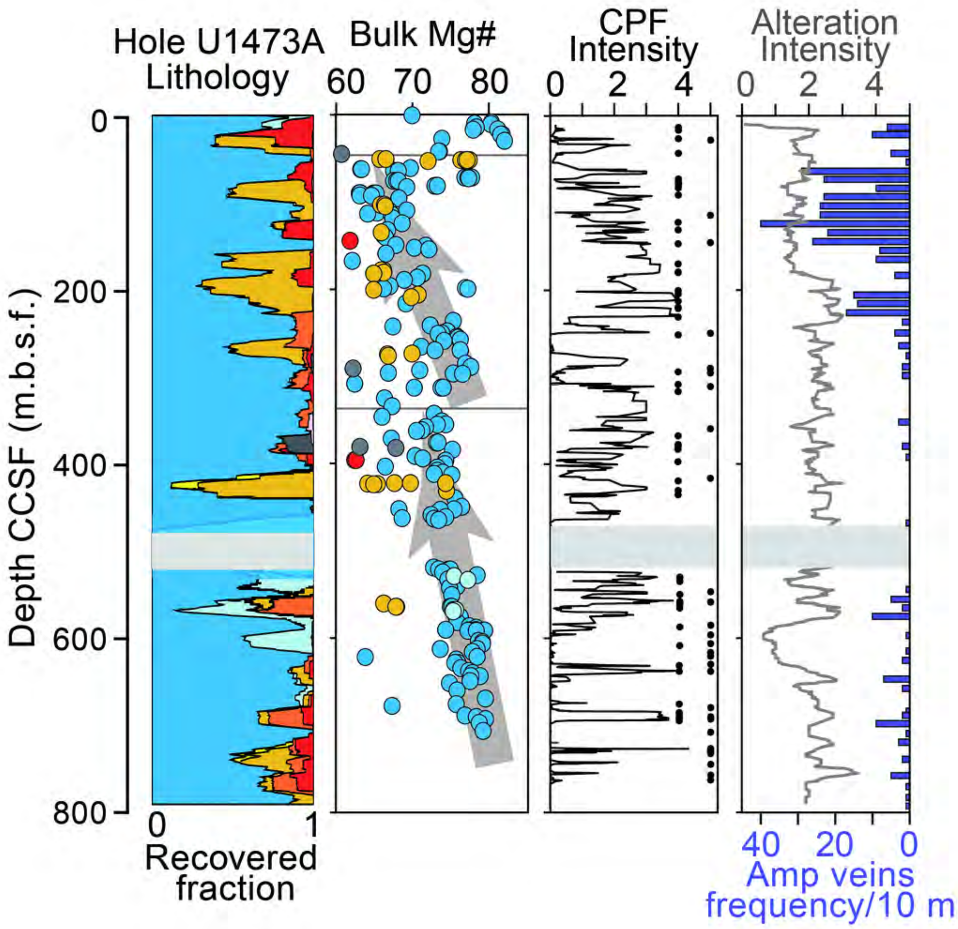

Figure 2 - Downhole characteristics of Hole U1473A. (From left to right) Downhole lithostratigraphic variations (relative abundances of rocks are averaged over 20 m) with olivine gabbro in dark blue, gabbro in light blue, disseminated oxide gabbro in yellow, oxide-bearing gabbro in orange, oxide gabbro in red, and diabase in grey; bulk-rock Mg# (Mg# = 100 × cationic (Mg/(Mg + Fe), with all Fe as Fe2+) of the recovered samples (dot colors represent the lithology as reported in the first column 'Hole U143A Lithology'); downhole intensity of crystal plastic fabrics (CPF): black line represents the 10 m running average of CPF intensity and black dots locate mylonites (CPF = 4) and ultramylonites (CPF = 5); 10 m running average of alteration intensity (grey line) and amphibole veins frequency (in blue) averaged over 10 m. CPF and alteration intensities values are from MacLeod et al., 2017.

90x87mm (300 x 300 DPI)

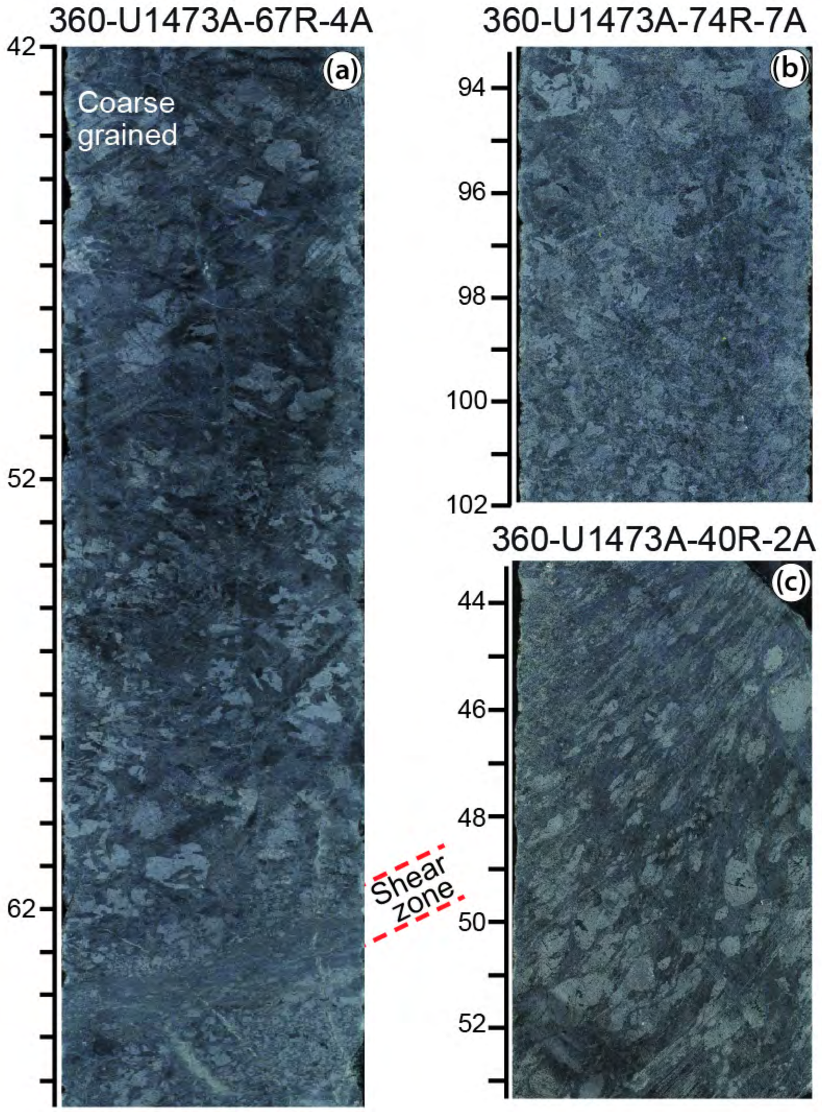

Figure 3 - Half core images of (a) coarse-grained olivine gabbro overall undeformed to slightly deformed showing a local mylonitic to ultramylonitic shear zone, (b) poikilitic undeformed olivine gabbro displaying isotropic magmatic fabric, (c) pervasive crystal-plastic deformation in an olivine gabbro. Images from onboard core scans (MacLeod et al., 2017).

74x97mm (300 x 300 DPI)

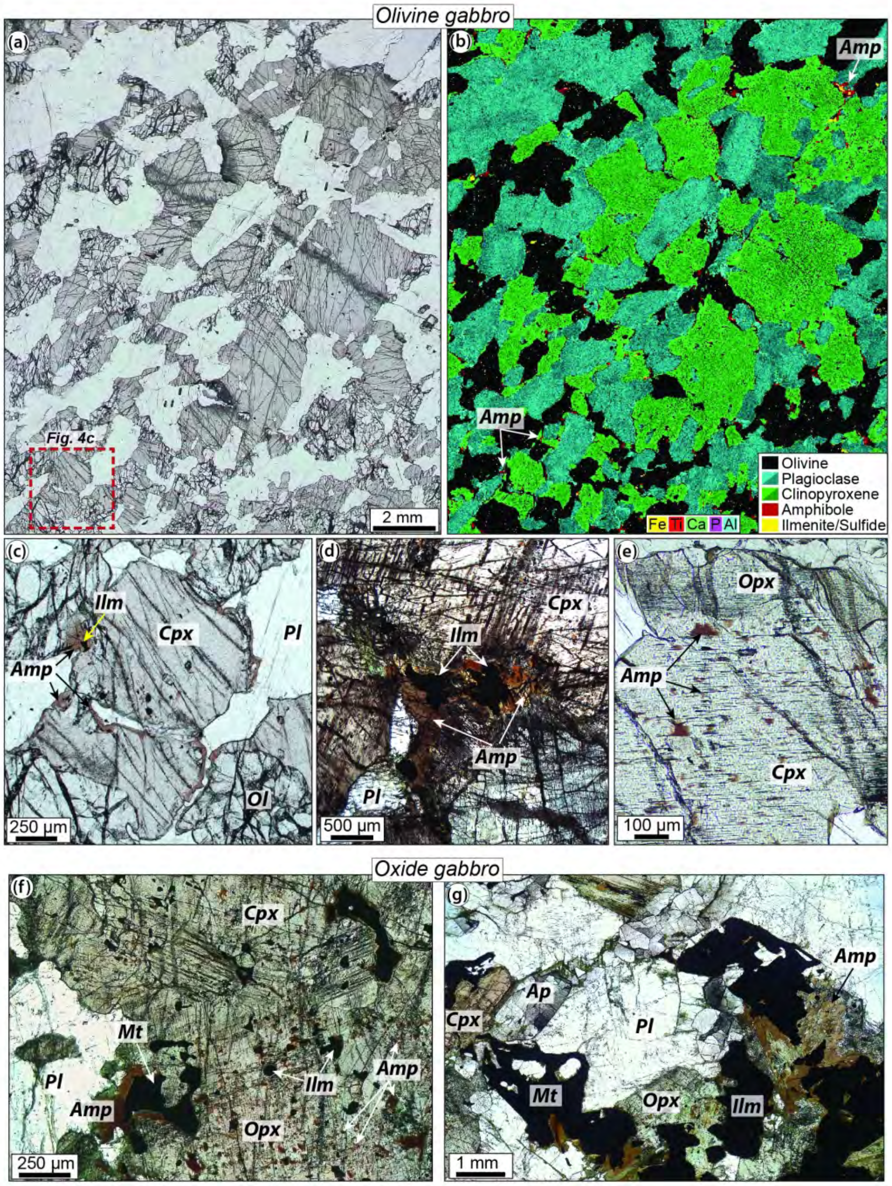

Figure 4 - Representative textures of undeformed olivine gabbro (samples (a-c) 360-U1473A-89R-6W, 4-9 cm and (d-e) 360-U1473A-89R-1W, 14-20 cm) and undeformed oxide gabbro (samples (f) 360-U1473A-81R-3W, 77-82 cm and (g) 360-U1473A-83R-1W, 13-20 cm). (a) Thin section scan of olivine gabbro under parallel-polarized light; the red box indicates the microphotograph in (c). (b) Composite Fe, Ti, Ca, P, Al compositional map of the thin section in (a); colour coding as reported in the image. (c) Close-up image from (a) showing films of interstitial brown amphibole (Amp), locally associated with small ilmenite (Ilm) crystals, along the grain boundaries of igneous phases (Ol – olivine, Pl – plagioclase, Cpx – clinopyroxene). (d) Interstitial amphibole associated with larger grains of ilmenite. (e) ‘Bleb-shaped’ amphibole in large clinopyroxene crystal rimmed by anhedral orthopyroxene (Opx). (f) Interstitial and ‘bleb-shaped’ amphibole associated with ilmenite and magnetite (Mt). (g) Large anhedral amphibole grains associated with ilmenite, magnetite, orthopyroxene and large euhedral crystals of apatite (Ap).

166x221mm (300 x 300 DPI)

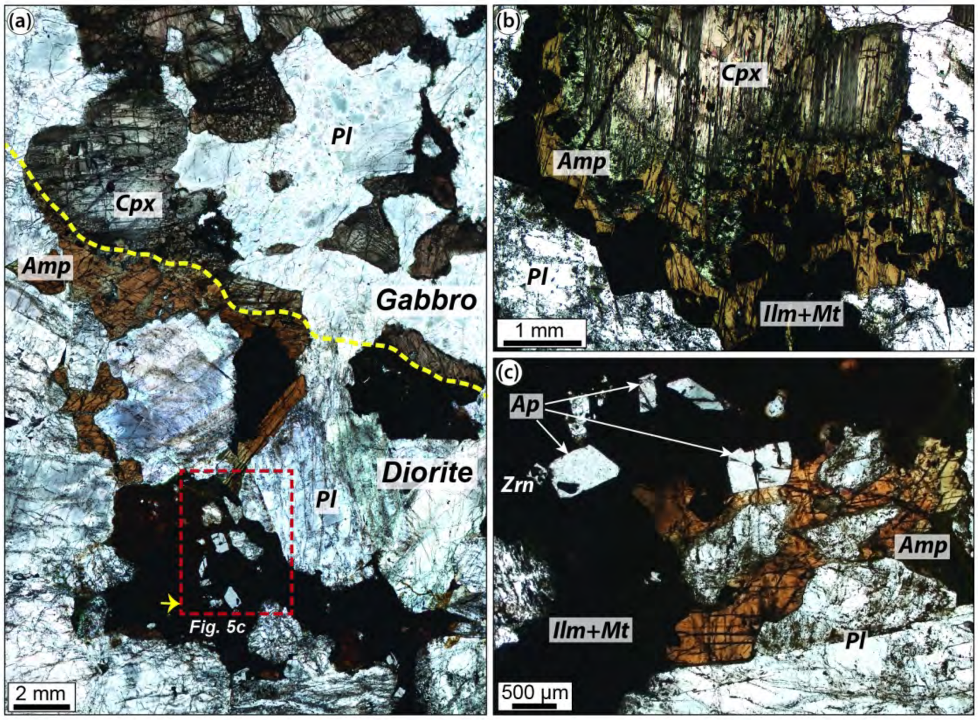

Figure 5 - Representative textures of dioritic intervals. (a) Contact between gabbro and diorite (yellow dotted line) marked by amphibole overgrowth on clinopyroxene of the host gabbro (sample 360-U1473A-39R-4W, 3-8 cm). The red box indicates the microphotograph in (c) and the yellow arrow points the top left corner in (c). (b) Corona of amphibole associated with ilmenite and magnetite partially enclosing and replacing clinopyroxene from the host gabbro at the contact with a dioritic interval in sample 360-U1473A-89R-3W, 108-110 cm. (c) Close-up image from (a) showing poikilitic amphibole in the core of the diorite; the amphibole encloses euhedral plagioclase, ilmenite, magnetite, apatite and zircon.

158x117mm (300 x 300 DPI)

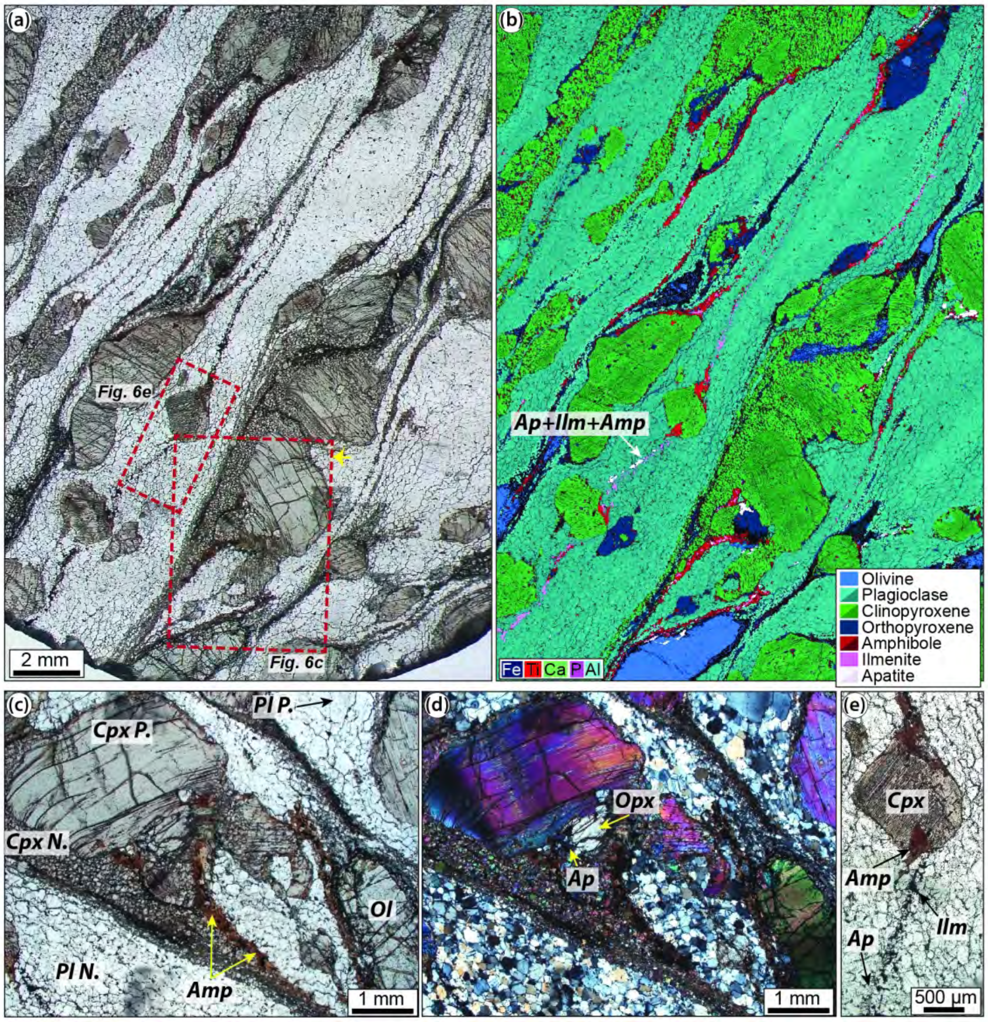

Figure 6 - Representative textures of granulite-facies mylonites. (a) Thin section scan (sample 360-U1473A-41R-6W, 23-29 cm) under parallel-polarized light; the red boxes indicate the microphotograph in (c) and (e). (b) Composite Fe, Ti, Ca, P, Al compositional map of the thin section in (a); color coding as reported in the image. Note that high Ti contents highlight the occurrence of brown amphibole. (c-d) Close-up images (c-parallel-polarized light, d-cross-polarized light) from (a) showing deformed clinopyroxene porphyroclast (Cpx P.) mantled by the clinopyroxene (Cpx N.) + amphibole neoblastic assemblage. Orthopyroxene and apatite occur in pressure shadows at the edge of the clinopyroxene porphyroclast. Plagioclase mostly occur as neoblasts (Pl N.) and only few porphyroclasts are preserved (Pl P.). (e) Close-up image from (a) showing amphibole + apatite + ilmenite thin isolated band, and the occurrence of elongated anhedral amphibole crystals in contact with a clinopyroxene porphyroclast.

166x171mm (300 x 300 DPI)

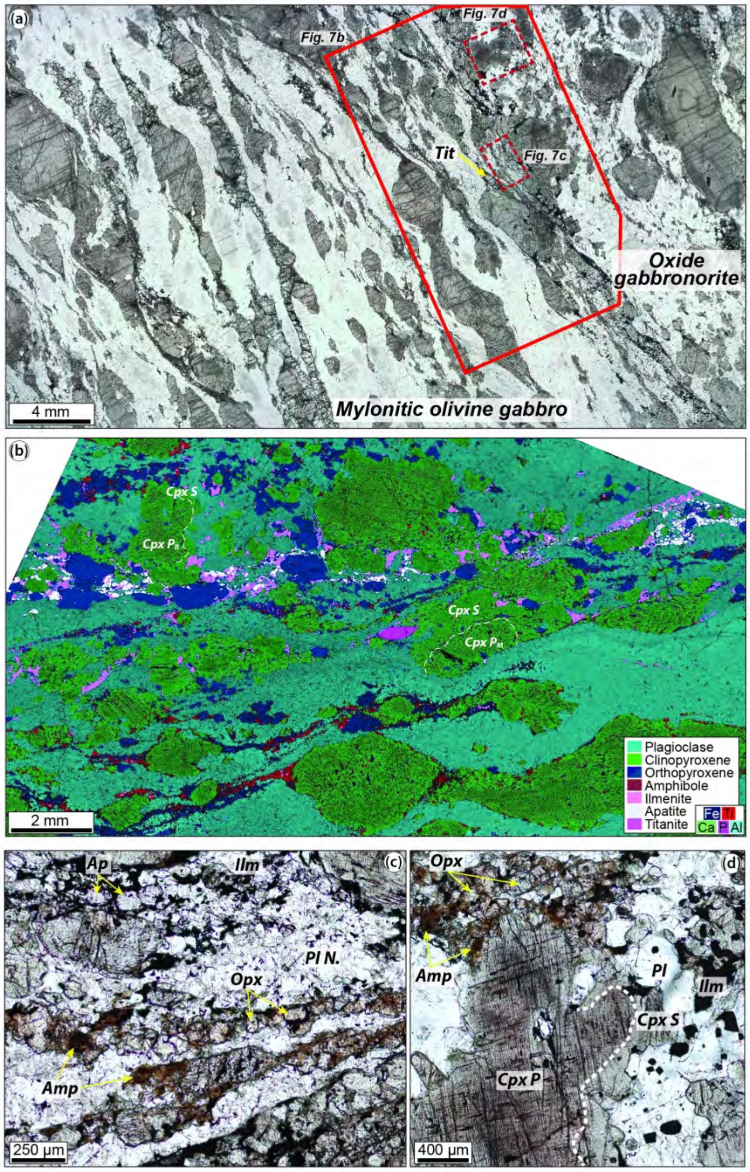

Figure 7 - Representative textures of mylonitic olivine gabbro (sample 360-U1473A-69R-1W, 23-28cm) crosscut by an oxide gabbronoritic band. (a) Thin section scan of the sample under parallel-polarized light; the full-line red box delineates the zone reported in (b), whereas the dashed red boxes indicate the microphotograph in (c) and (d). Note the euhedral crystal of titanite within the oxide gabbronoritic band. (b) Composite Fe, Ti, Ca, P, Al compositional map of zone highlighted in (a); colour coding as reported in the image. Note that high Ti contents highlight the occurrence of brown amphibole, whereas combined Ti and Fe (pink colour) and P and Al (whitish colour) mark the occurrence of ilmenite and apatite, respectively. Porphyroclastic clinopyroxene from the host mylonite (Cpx PM) and in the band (Cpx PB) are overgrown by secondary clinopyroxene (Cpx S). (c) Close-up image showing neoblastic plagioclase (Pl N) + ilmenite + apatite and brown amphibole + orthopyroxene levels. (d) Close-up image showing clinopyroxene porphyroclast (Cpx P) mantled by anhedral secondary clinopyroxene (Cpx S; white dashed line marks the contact). At top left corner, an aggregate of neoblastic orthopyroxene + amphibole is also present.

165x250mm (300 x 300 DPI)

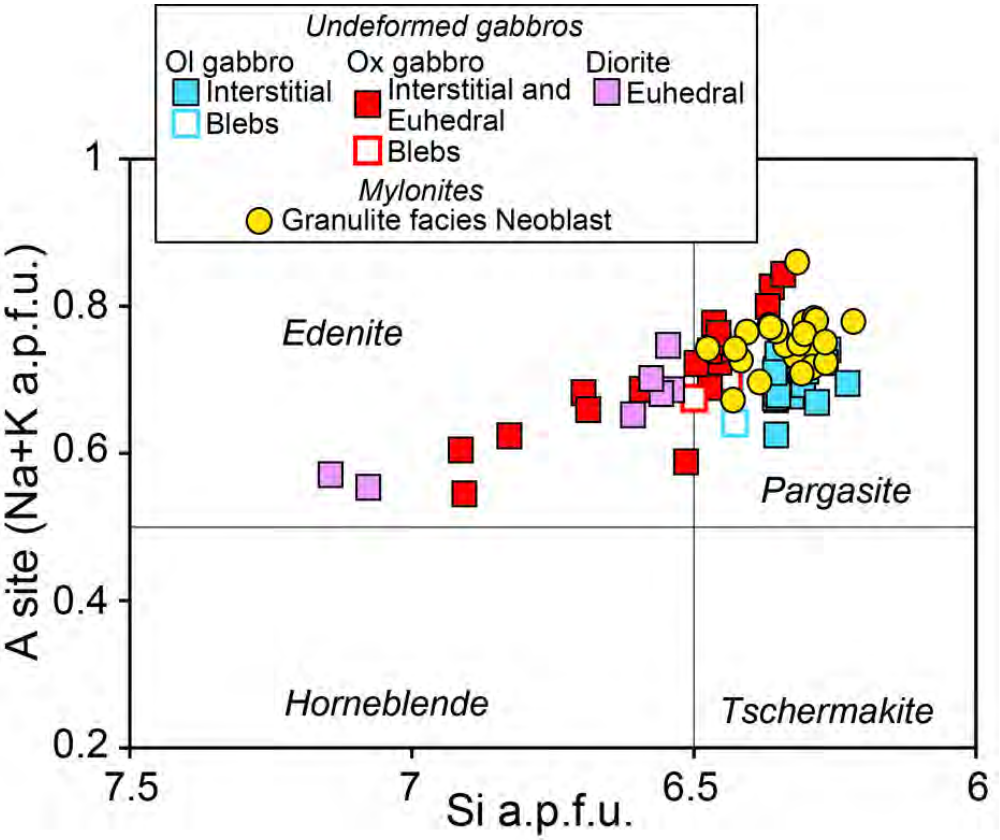

Figure 8 - Si a.p.f.u. (atom per formula unit) versus [Na + K] a.p.f.u. in brown amphibole from olivine gabbros, oxide gabbros, diorites and granulite-facies mylonites in IODP Hole U1473A. Amphibole classification after Leake et al. (1997). Structural formulae of amphibole were determined by assuming all iron as Fe2+, positive charge = 46, and 23 oxygens.

78x65mm (300 x 300 DPI)

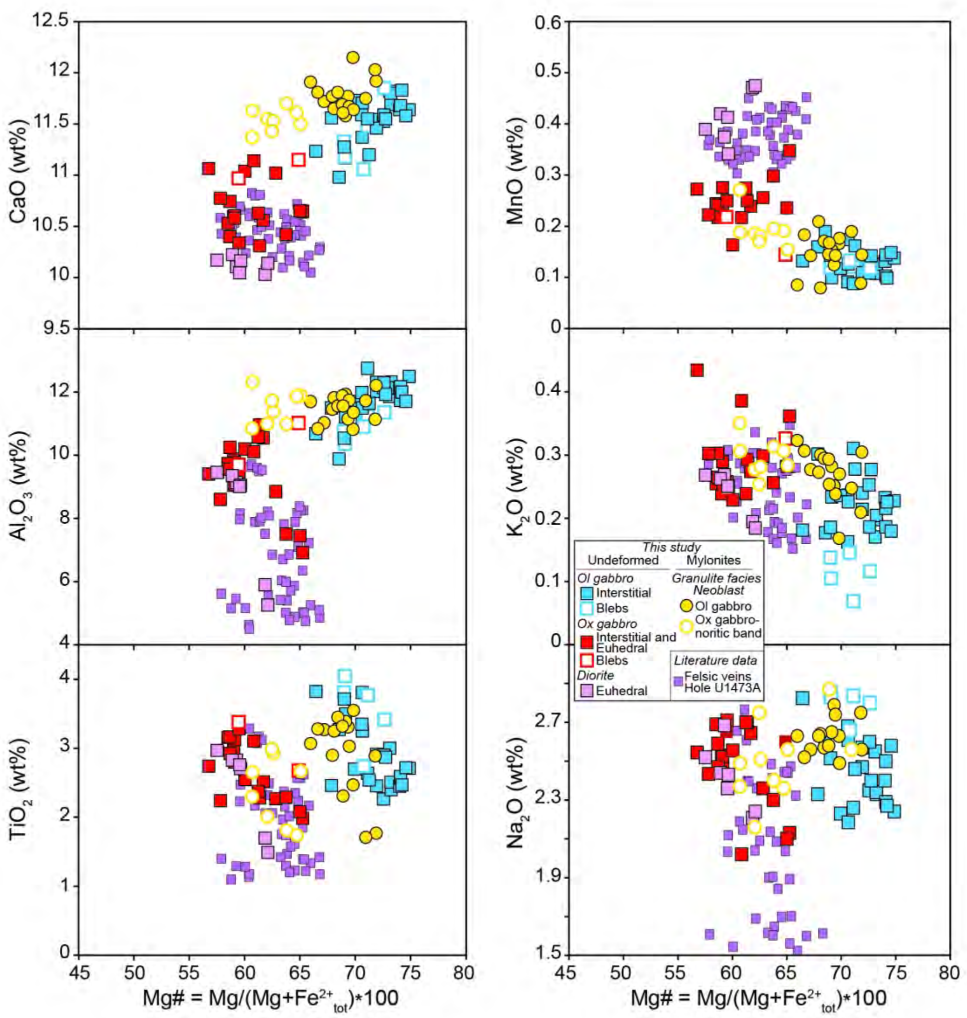

Figure 9 – Major element compositions of brown amphiboles. Amphiboles are subdivided according to lithology and textures as reported in the legend. The composition of amphiboles in felsic veins from IODP Hole U1473A (Nguyen et al., 2018) is also reported for comparison. In granulite-facies mylonites, we distinguished amphibole in the apatite-ilmenite rich band (69-1; from sample U1473A-69R-1W, 23-28cm) from amphibole in the rest of the mylonitic intervals (41-6; mainly from sample U1473A- 41R-6W, 23-29 cm).

164x172mm (300 x 300 DPI)

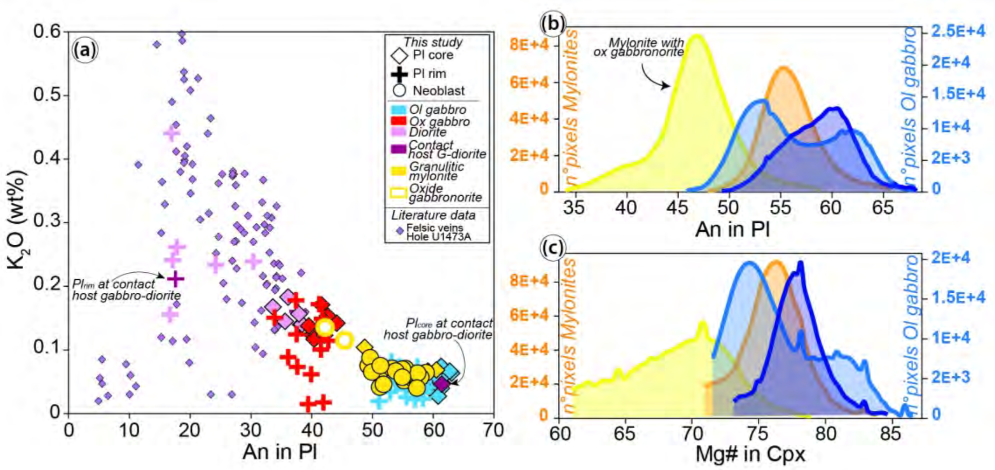

Figure 10 – (a) An versus K2O (wt%) contents in plagioclase from olivine gabbros, oxide gabbros, diorites and granulite-facies mylonites in IODP Hole U1473A. Plagioclase core and plagioclase rim refer to euhedral/subhedral plagioclase in gabbros and plagioclase porphyroclasts in mylonites. The composition of plagioclase in felsic veins from IODP Hole U1473A (Nguyen et al., 2018) is also reported for comparison. (b) and (c) Histograms of distribution of An contents in plagioclase (b) and Mg# in clinopyroxene (c) obtained after statistical analysis (QACD tool) on chemical maps. Blu colours refer to olivine gabbros, whereas yellow colours refer to mylonitic olivine gabbros.

161x77mm (300 x 300 DPI)

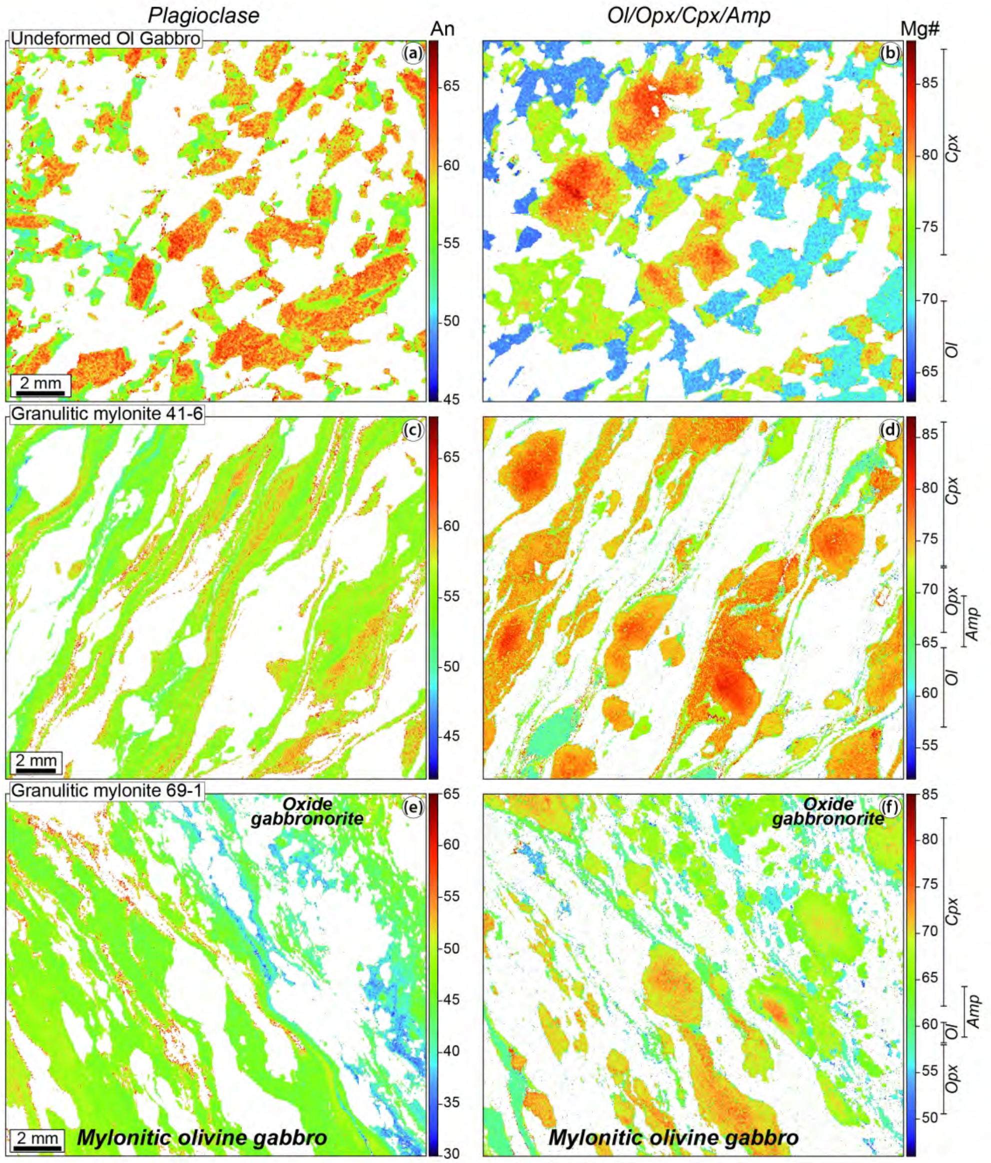

Figure 11 – Anorthite (An) map in plagioclase (a-c-e) and maps of Mg# in olivine, pyroxenes and amphibole (b-d-f). (a) and (b) sample 360-U1473A-89R-6W, 4-9 cm reported in Figure 4. (c) and (d) sample 360-U1473A- 41R-6W, 23-29 cm reported in Figure 6. (e) and (f) sample 360-U1473A-69R-1W, 23-28cm reported in Figure 7.

192x227mm (300 x 300 DPI)

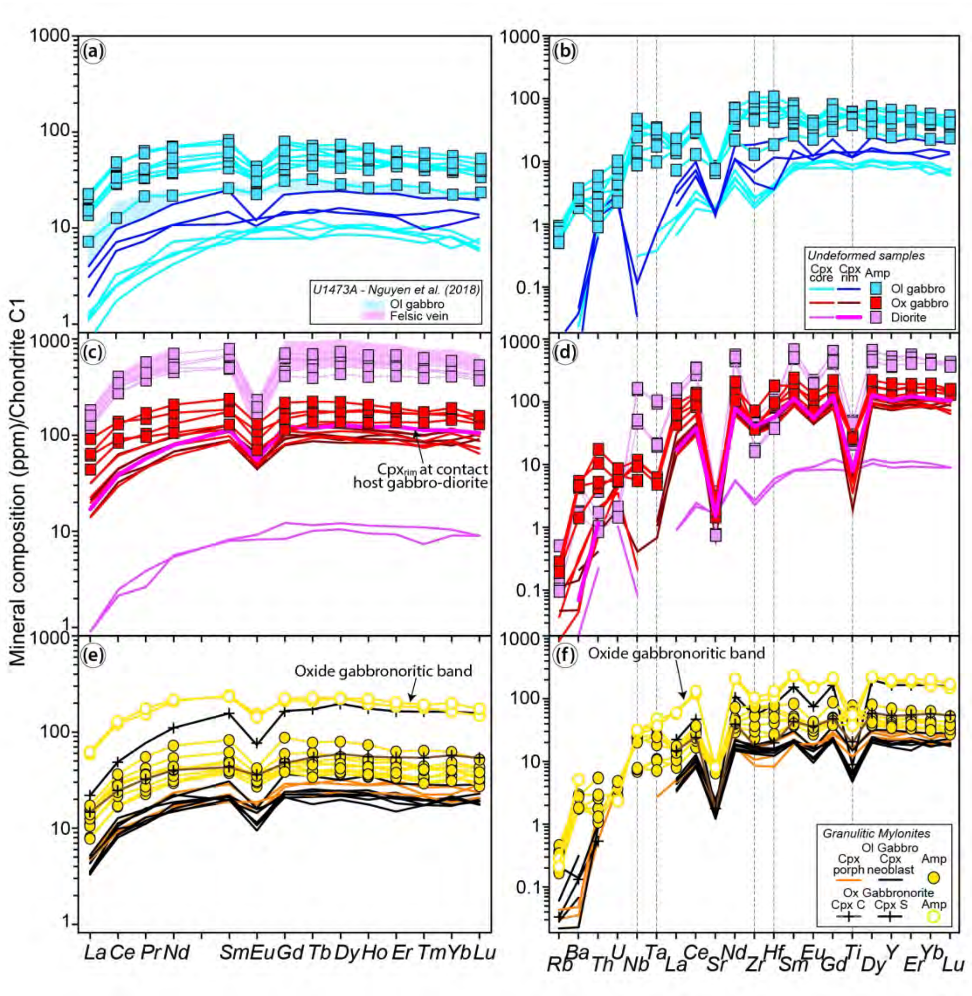

Figure 12 – Chondrite-normalized Rare Earth Element (REE) concentrations (a,c,e) and extended trace element spider diagrams (b,d,f) of brown amphibole and coexisting clinopyroxene in undeformed olivine gabbros (a,b), oxide gabbros and diorites (c,d) and mylonitic olivine gabbros (e,f) from Hole U1473A. Compositional fields of brown amphiboles in other olivine gabbros and felsic veins from the same hole (Nguyen et al., 2018) are also reported for comparison. Normalizing values are after Sun and McDonough (1989).

171x170mm (300 x 300 DPI)

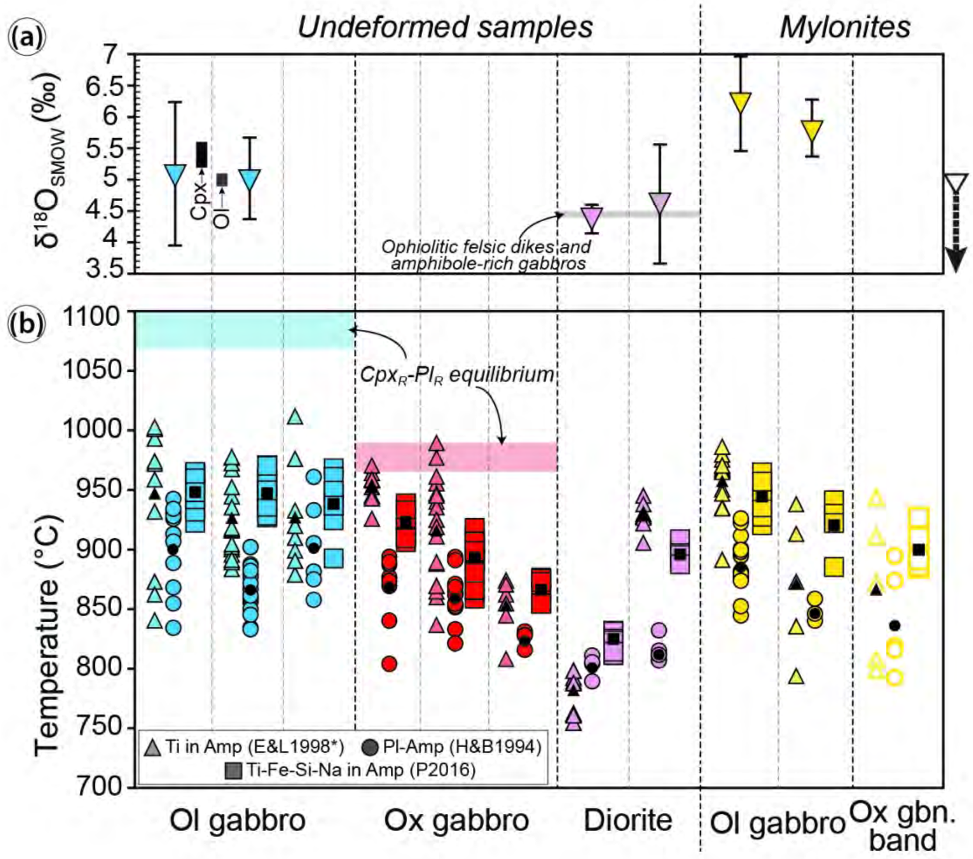

Figure 13 – (a) Average values (per sample with 2σ error bar) of in situ δ18O values of brown amphiboles in undeformed olivine gabbros (light blue) and diorites (pink) and in mylonites (yellow). The δ18O compositions of magmatic clinopyroxene (Cpx, black box) and olivine (Ol, dark grey box) in olivine gabbros (Gao et al., 2006) and hydrothermal hornblende in veins (Alt & Bach, 2006; dark grey arrow on the right) from the adjacent Hole 735B are reported. For comparison, we report the δ18O values of amphibole in felsic dikes and amphibole-rich gabbros from the Ligurian ophiolites (Tribuzio et al., 2014; light grey field). (b) Equilibrium temperature estimates for crystallization of brown amphibole in olivine gabbros, oxide gabbros and diorites, and for ductile deformation and development of granulite-facies mylonitic intervals in IODP Hole U1473A. Amphiboles from the granulite-facies mylonites were subdivided as reported in Figure 9, and temperature estimates were determined for neoblastic grains exclusively. Amphibole-plagioclase geothermometer (Holland & Blundy, 1994 [H&B1994]) and two single-amphibole geothermometer (Ti-Fe-Si-Na in amphibole (Amp) by Putirka, 2016 [P2016] and Ti-in amphibole by Hannover group [E&L1998*]; see text for further details) were used. Equilibrium temperatures between clinopyroxene and plagioclase rims (CpxR and PlR) determined using the geothermometer from Sun et al. (2017) for olivine gabbros (blue box) and oxide gabbros (red box) are also reported for comparison. Each column corresponds to a single sample.

113x103mm (300 x 300 DPI)

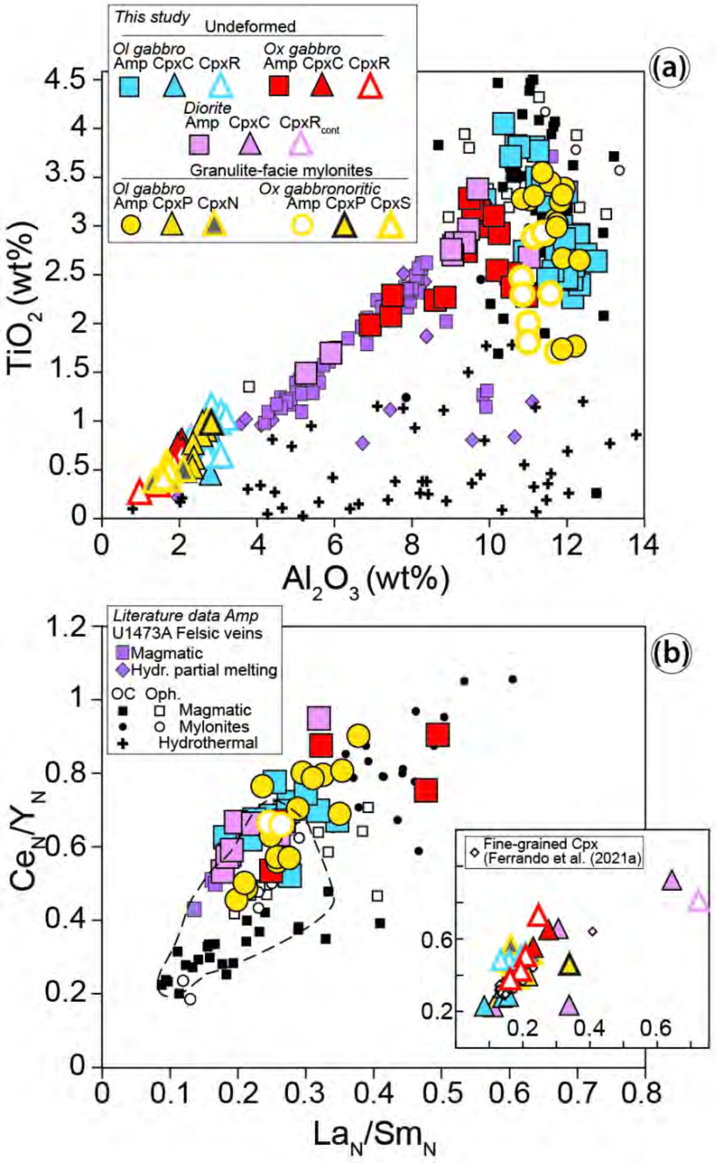

Figure 14 – Major and trace element covariations in coexisting brown amphibole and clinopyroxene from undeformed olivine gabbros, oxide gabbros and diorites and mylonitic olivine gabbros sampled in Hole U1473A. (a) TiO2 (wt%) versus Al2O3 (wt%) contents and (b) CeN/YN versus LaN/SmN (where N = Chondrite normalized values) are compared with compositions of amphibole in felsic veins from the same hole (felsic veins of magmatic origin from Nguyen et al. (2018) and Ma et al. (2020) (Type I); felsic veins as products of hydrous partial melting are Type II of Ma et al.(2020)) and magmatic amphiboles and hydrothermal amphiboles from oceanic spreading centers (Coogan et al., 2001; Gillis & Meyer, 2001; Miranda & John, 2010; Sanfilippo et al., 2019; Harigane et al., 2019) and ophiolitic analogues (Tribuzio et al., 1995, 1999, 2000). The dotted line in (b) defines the compositional field of the studied clinopyroxene, which are reported in the bottom-right inset. In the inset we also plot the compositions of clinopyroxene from fine-grained intervals of olivine gabbros sampled in the same Hole U1473A.

82x127mm (300 x 300 DPI)

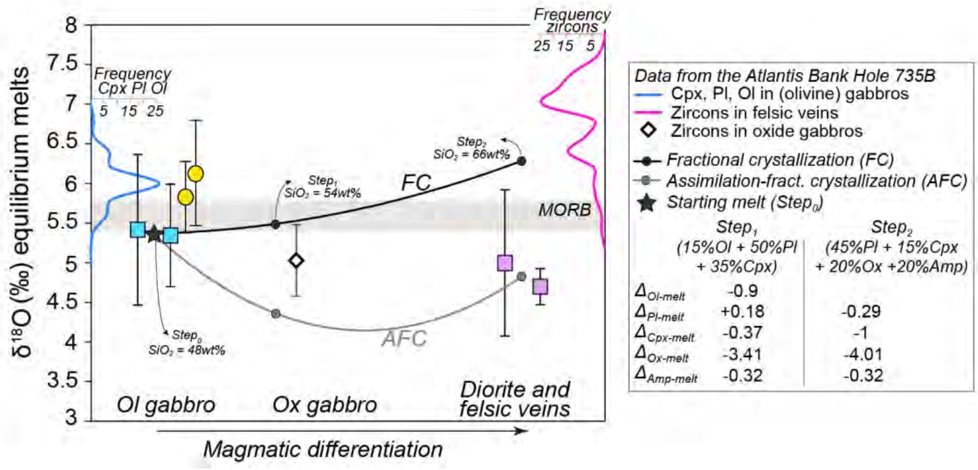

Figure 15 – δ18O values of computed melts in equilibrium with brown amphibole from olivine gabbros (undeformed and mylonitic) and diorites in Hole U1473A (this study; symbols and colour codes as in Fig. 14) compared with melts in equilibrium with clinopyroxene (Cpx), olivine (Ol) and plagioclase (Pl) from gabbros (blue histogram; Gao et al., 2006) and with zircons from oxide gabbros (diamond symbol) and felsic veins (pink histogram) (Pietranik et al., 2017) in Hole 735B at the Atlantis Bank OCC. The field of MORB (d18O = 5.6 ± 0.2) is from Eiler (2001). The δ18O values of calculated equilibrium melts are compared with fractional crystallization (FC) and assimilation-fractional crystallization (AFC; see DePaolo, 1981) models. The composition of the starting melt for both models is the computed melt in equilibrium with average δ18O values of pargasites in the studied undeformed olivine gabbros. Two steps of F=50% were modelled following the approach in France et al. (2016); Step1 reproduces melt composition after crystallization of Ol+Pl+Cpx and Step2 after crystallization of Pl+Cpx+Ox+Amp (mineral modes are reported in the legend) with predicted SiO2 contents of 54 and 66wt%, respectively, which are comparable with hypothetic compositions of oxide gabbros and diorites parental melts. The assimilated material is set as oceanic crust altered at high temperature conditions and thus with low δ18O signatures (~3 ‰ ; Stakes, 1991; Alt & Bach, 2006); the ratio crystallized/assimilated masses is 2. Used fractionation factors (Δmineral-melt) are reported in the legend; because they are dependent on temperature, the Δmineral-melt were derived at suitable conditions for each lithological group (from Muehlenbachs & Byerly, 1982; Zhao & Zheng, 2003; Bindeman, 2008; France et al., 2016). Δzircon-melt is derived from Lackey et al. (2008) with Δzircon-melt = 0.75 ‰ for oxide gabbros, and Δzircon-melt = 1.5 ‰ for diorites and felsic veins.

140x66mm (300 x 300 DPI)

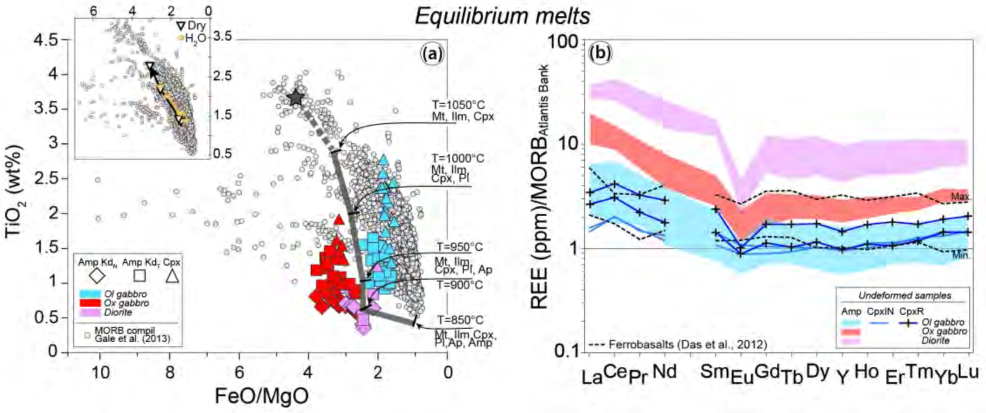

Figure 16 – Computed melts in equilibrium with amphiboles and clinopyroxene from all undeformed lithologies. (a) TiO2 (wt%) contents versus FeO/MgO ratios are compared with the database of MORBs from Gale et al. (2013) and the magmatic crystallization experiments of a ferrobasaltic melt (Koepke et al., 2018), for which we report temperature and mineral assemblage at each crystallization step (Mt = magnetite, Ilm = ilmenite, Cpx = clinopyroxene, Pl = plagioclase, Ap = apatite, Amp = amphibole). In the inset we also report the liquid line of descent of a primitive MORB, experimentally reproduced at anhydrous (dry) and hydrous (H2O) conditions (Husen et al., 2016). Note that using partition coefficients from Nandedkar et al. (2016) (KdN) and Tiepolo et al. (2007) (KdT) to calculate melts in equilibrium with amphibole yield similar results. (b) Atlantis Bank MORB-normalized (average MORB composition from Coogan et al., 2004) REE contents in melts in equilibrium with amphiboles from the three undeformed lithologies and clinopyroxene from olivine gabbros; the melts in equilibrium with clinopyroxene from the oxide gabbros have not been calculated because of the uncertainty in the choice of the clinopyroxene/melt partition coefficients in chemically evolved systems. The dotted lines mark the minimum (Min.) and maximum (Max.) REE concentrations in ferrobasalts from the Indian Ridge (Das et al., 2012). CpxIN = analyses performed at ~50m form the clinopyroxene rim (CpxR).

180x76mm (300 x 300 DPI)

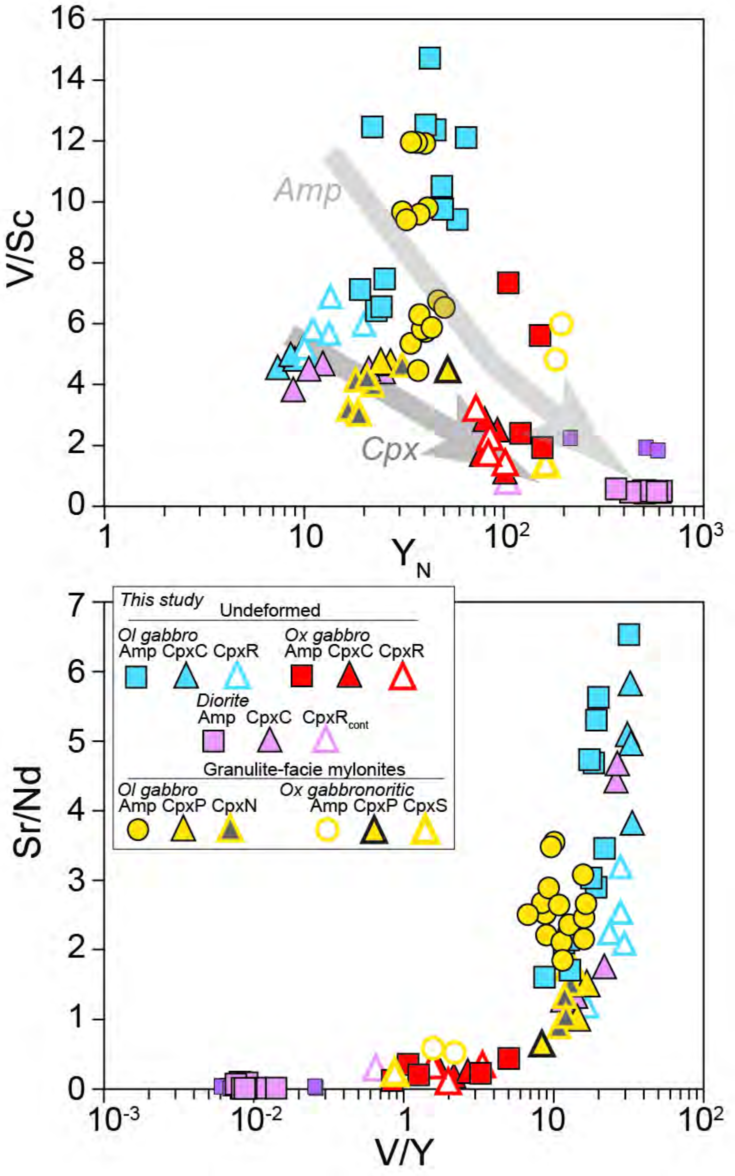

Figure 17 – (a) V/Sc vs Chondrite-normalized Y and (b) Sr/Nd vs V/Y covariations in clinopyroxene and amphibole from the undeformed and deformed lithologies selected for this study.

73x114mm (300 x 300 DPI)